

Variations in the morphology of porosity in the Boom Clay Formation: insights from 2D high resolution BIB-SEM imaging and Mercury injection Porosimetry

S. Hemes^{1,*}, G. Desbois¹, J.L. Urai¹, M. De Craen² & M. Honty²

¹ Structural Geology, Tectonics and Geomechanics, Energy and Mineral Resources Group, RWTH Aachen University, Lochnerstrasse 4-20, 52056 Aachen, Germany

² SCK-CEN, Belgian Nuclear Research Centre, Environment, Health and Safety Institute, Waste & Disposal Expert Group, Boeretang 200, 2400 Mol, Belgium

* Corresponding author. Email: s.hemes@ged.rwth-aachen.de

Manuscript received: January 2013, accepted: September 2013

Abstract

Boom Clay is considered as one of the potential host rocks for the disposal of high level and/or long lived radioactive waste in a geological formation in Belgium (Mol study site, Mol-1 borehole) and the Netherlands. The direct characterisation of the pore space is essential to help understand the transport properties of radionuclides in argillaceous materials.

This contribution aims to characterise and compare the morphology of the pore space in different Boom Clay samples, representing end-members with regard to mineralogy (i.e. clay content) and grain-size distribution of this formation. Broad ion beam (BIB) cross-sectioning is combined with SEM imaging of porosity and Mercury injection Porosimetry (MIP) to characterise the variability of the pore space in Boom Clay at the nm- to μm -scale within representative 2D areas and to relate microstructural observations to fluid flow properties of the bulk sample material. Segmented pores in 2D BIB surfaces are classified according to the mineralogy, generating representative datasets of up to 100,000 pores per cross-section.

Results show total SEM-resolved porosities of 10-20 % and different characteristic mineral phase internal pore morphologies and intra-phase porosities.

Most of the nano-porosity resides in the clay matrix. In addition, in the silt-rich samples, larger inter-aggregate pores contribute to a major part of the resolved porosity. Pore-size distributions within the clay matrix suggest power-law behaviour of pore areas with exponents between 1.56-1.74. Mercury injection Porosimetry, with access to pore-throat diameters down to 3.6 nm, shows total interconnected porosities between 27-35 Vol.-%, and the observed hysteresis in the MIP intrusion vs. extrusion curves suggests relatively high pore-body to pore-throat ratios in Boom Clay. The difference between BIB-SEM visible and MIP measured porosities is explained by the resolution limit of the BIB-SEM method, as well as the limited size of the BIB-polished cross-section areas analysed. Compilation of the results provides a conceptual model of the pore network in fine- and coarse-grained samples of Boom Clay, where different mineral phases show characteristic internal porosities and pore morphologies and the overall pore space can be modelled based on the distribution of these mineral phases, as well as the grain-size distribution of the samples investigated.

Keywords: Boom Clay, broad-ion-beam milling, Mercury injection Porosimetry, pore morphologies, pore-size distribution, SEM-imaging

Introduction

Due to its low hydraulic conductivity ($\sim 1 \cdot 10^{-12}$ m/s), i.e. low intrinsic permeability ($\sim 1 \cdot 10^{-17}$ m²) and good sealing capacities (Neuzil, 1994; De Craen et al., 2004), the Boom Clay is being considered as one of the potential host rock materials for the

disposal of high and medium level radioactive waste in a geological formation in Belgium and the Netherlands (Gens et al., 2003; Verhoef & Schröder, 2011; Verhoef et al., 2011; ONDRAF/NIRAS, 2011). Furthermore the material shows very good sorption capacities for radionuclides and high stability over a geological timescale. It has been shown that the transport of

radionuclides in the Boom Clay Formation is mainly controlled by diffusion through the accessible pore space (Ortiz et al., 2002; Aertsens et al., 2008). Thus, the detailed characterisation of pore morphologies, including size, shape, orientation and connectivity of the pores, down to the nm-scale, is important to gain a fundamental understanding of the transport of radionuclides.

The Boom Clay has been investigated intensively since 1974 (by SCK-CEN) and since 1996 is studied in-situ in an underground research laboratory (HADES – ‘High Activity Disposal Experimental Site’) at the Mol-Dessel research site (Belgium). Therefore, its bulk chemical composition and bulk physical and chemical properties are very well known. Classical studies include mineralogical, geochemical and granulometric investigations, comprising solid phase mineralogical characterisation via X-ray diffraction (Vandenbergh, 1974, 1978; Declerck et al., 1983; Laenen, 1997; Zeelmaekers, 2011), Fourier transform infrared spectroscopy (Wouters et al., 1999; FUNMIG, 2008), thermal gravimetric analysis (FUNMIG, 2008), surface area analysis (Baeyens et al., 1985; Honty et al., 2010) and cation exchange capacity measurements (Baeyens et al., 1985; Griffault et al., 1996; Honty et al., 2010). For elemental analysis, atomic absorption and emission spectroscopy (AAS/AES), X-ray fluorescence, inductively coupled plasma mass spectrometry (ICP-MS) and instrumental neutron activation analysis (INAA) were applied (e.g. Declerck et al., 1983, Declerck & Viaene, 1993; Laenen, 1997; De Craen et al. 2000; Zeelmaekers, 2011).

The microstructure and pore space of the Boom Clay have been studied to a much lower extent. Standard bulk porosity measurements include Mercury injection Porosimetry (MIP) (Al-Mukhtar et al., 1996; Boisson, 2005; Dehandschutter et al., 2005), water content porosity measurements (e.g. Merceron, 1994; Boisson, 2005) and radionuclide (HTO) diffusion experiments (e.g. Aertsens et al., 2005a, b; Bruggeman et al., 2009). Alternative methods, such as density difference calculations (FUNMIG, 2008) or gas generation and migration experiments (Ortiz et al., 2002) have also been used. However, all these methods yield only indirect information on the morphology and connectivity of pore space. Direct microstructural studies on Boom Clay, at the scale of pores and grains, were done using scanning electron microscopy (SEM) on broken surfaces of Boom Clay (Baeyens et al., 1985; Al Mukhtar et al., 1996; De Craen et al., 1999; Romero et al., 1999; Hildenbrand & Urai, 2003), but suffered from difficulties in the interpretation of the images, due to the roughness of the surfaces. Recent developments in the field of micro-focus X-ray computed tomography (μ -CT) (Bésuelle et al., 2006; Jin, 2007; Bugani et al., 2009; Sok et al., 2009; Bell et al., 2011; Cnudde et al., 2011) allow describing the 3D fabrics of clay materials and its evolution under load, but the resolutions achieved are not good enough to resolve porosity. The emergence of ion-beam milling tools, like focussed (FIB) and broad-ion-beam (BIB) cross-sectioning (Holzer et al., 2006, 2007, 2010; Loucks et al., 2009; Desbois et al., 2010a, b; 2011a, b; Holzer & Cantoni, 2012) led to an important progress in imaging

microstructures and porosity in argillaceous materials, down to the nm-scale resolution. FIB serial cross-sectioning allows reconstructing 3D microstructures (Van Geet et al., 2008; Heath et al., 2011; Keller et al., 2011). A problem in integrating these results is the gap in resolutions and sizes of analysed sample volumes between serial FIB-SEM nano-tomography (nm-scale resolution, visualising sample volumes $<1,000 \mu\text{m}^3$) and μ -CT ($> \mu\text{m}$ -scale resolution, visualising volumes in the cm^3 to mm^3 range). One approach to overcome this problem is to combine BIB-milling with high resolution SEM imaging, achieving a resolution down to the nm-scale on representative sample areas of several thousands of μm^2 up to 1mm^2 size (Desbois et al., 2009; Loucks et al., 2009 and 2012; Klaver et al., 2012; Houben et al., 2013). To quantify microstructures, the principle of fractal geometry is often used, and was first applied to geological materials by Friesen & Mikula (1987); it was furthermore found adequate to describe the porosity in different sandstones, shales and granites (Ruffett et al., 1991). A material property can be described as fractal, if it behaves in the same way, regardless of the scale of measurement or observation. Using power-laws is one way to describe fractal size distributions and a possibility to model these distributions. Many naturally occurring size distributions were found to follow a power-law behaviour (Zipf, 1949; Bak, 1996) and recently it has been shown that the size distribution of pore-areas in clayey materials can be modelled using power-laws (Desbois et al., 2009; Klaver et al. 2012; Houben et al., 2013).





This study aims to characterise and compare the morphology of the pore space in different Boom Clay samples, representing end-members with regard to mineralogical composition and grain-size distribution of the Boom Clay Formation at the Mol-1 borehole (Belgium). BIB cross-sectioning is combined with high resolution SEM-imaging to characterise the variability of the pore space in Boom Clay at the nm- to μm -scale resolution, within areas, which are representative of the material's mineralogical composition, grain-size distribution and porosity, at the scale of observation. Pores are segmented from secondary electron (SE) images and classified according to the mineralogy, generating statistically representative datasets of up to 100,000 pores per image and sample cross-section. Mercury injection Porosimetry (MIP) provides data relating microstructural information to the bulk transport properties of the sample material. The compilation of the results yields a conceptual model of the pore space in fine- and coarse-grained Boom Clay samples.

Samples and Methodology

Samples

In the present study four samples from the Mol-1 borehole (Mol-Dessel research site for radioactive waste disposal, Belgium) were investigated (ON-Mol-1-168, ON-Mol-1-184, ON-Mol-1-196 and ON-Mol-1-253). The main characteristics of the samples are

Table 1. Characteristics of samples investigated (mineralogical data from Zeelmaekers, 2011; grain-size data provided by SCK-CEN).

Sample ID	Depth of origin (m below sea level TAW)	Formation member	Median grain diameter (μm)	Notation	Clay content (dry wt.-%)	Symbol	Reference used in this contribution
ON-M:ll-1-168	168	Boeretang	31.3	Coarse-grained	34		EZE52
ON-M:ll-1-184	184	Boeretang	1.4	Fine-grained	61		EZE54
ON-M:ll-1-196	196	Putte	1.4	Fine-grained	51		EZE55
ON-M:ll-1-253	253	Belsele-Waas	15.6	Coarse-grained	28		EZE64

summarised in Table 1 and in the present study, sample names from Edwin Zeelmaekers PhD thesis (2011) are used for reference. The four samples were chosen to represent end-members with regard to mineralogical composition and grain-size distribution of the 'EZE' (Zeelmaekers, 2011) sample series (Figs 1 and 2). Mineralogical data are based on XRD and bulk rock analysis from Zeelmaekers (2011). Grain-size distributions were measured by SCK-CEN at KU Leuven using a 'Micromeritics SediGraph5100' analyser. Prior to the analysis, carbonates, Fe-oxides and hydroxides, as well as organic matter were removed, applying a modified Jackson (1985) treatment, using HCl, oxalic acid and H_2O_2 , respectively.

BIB-SEM method

Sample preparation

Samples for BIB milling are $\sim 10 \times 5 \times 2$ mm in size and were cut from core samples of 10 cm diameter using a razorblade. The cores of samples EZE54, EZE55 and EZE64 were received in a natural, hydrated state, whereas sample EZE52 had already been oven dried by SCK-CEN at 60°C for 48 hours. The hydrated samples were dried carefully prior to the BIB-SEM investigations, since otherwise the high vacuum applied during BIB-milling and SEM-imaging would lead to a too fast extraction of water from the samples, possibly causing critical damage to the original sample microstructure. Nevertheless, we cannot fully exclude the potential creation of drying artefacts, due to sample volume changes during drying, which will be discussed later on in this contribution. Samples EZE54, EZE55 and EZE64 were gradually oven dried, increasing the temperature stepwise $\sim 5\text{--}10^\circ\text{C}$ per day from room temperature ($\sim 23^\circ\text{C}$) up to a maximum temperature of 100°C over a period of 10 days. Samples were weighed throughout the drying experiment and water content porosities calculated based on the bulk sample grain densities ($2.56\text{--}2.63\text{ g/cm}^3$) and the density of the pore fluid (1.02 g/cm^3) (De Craen et al., 2004). In addition, sample dimensions were measured to estimate the shrinkage of the samples due to drying. Dried samples were glued onto sample holders suitable for broad ion beam (BIB) polishing using cyanoacrylate glue and pre-polished using carbide papers (P500-2400, ISO/FEPA Grit, from 30.2 down to $8.4\ \mu\text{m}$ grain size, respectively). A JEOL SM-09010 stand-alone Argon beam polisher is used to produce high quality, damage-free cross-sections for

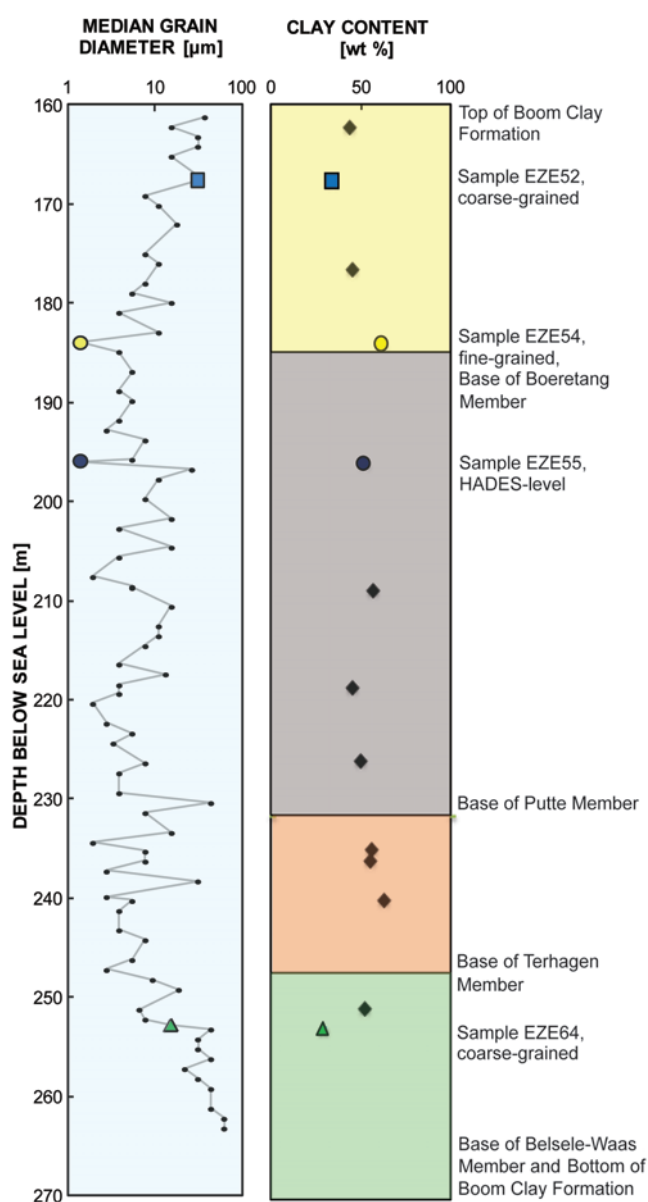


Fig. 1. Location of samples from the 'Edwin Zeelmaekers' (EZE; Zeelmaekers, 2011) sample series from the Mol-1 borehole (Mol-Dessel research site for radioactive waste disposal, Belgium), along with the borehole stratigraphy. Samples investigated in this contribution (EZE52, EZE54, EZE55 and EZE64) are indicated by coloured symbols (cf. Table 1). The depth of origin of the samples (m below sea-level = TAW) is shown, together with the median grain diameter [μm], the clay-content (dry wt.-%) and the main stratigraphic formation members.

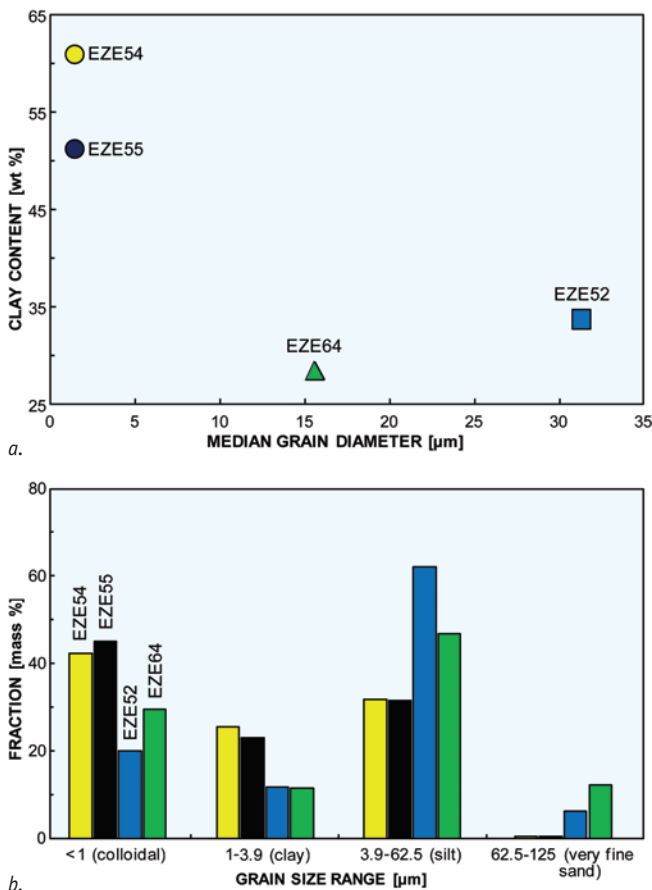


Fig. 2. a. Clay content (dry wt.-%) vs median grain diameter (μm) of samples investigated; b. fraction (%) of different grain-size ranges, after 'Wentworth Classification' (Wentworth, 1922; data from Zeelmaekers, 2011).

high-resolution SEM investigations (Desbois et al., 2009; Klaver et al., 2012; Houben et al., 2013). BIB polishing was performed for 7.45 hours at 6 kV and 150 μA , resulting in cross-sections of $\sim 1\text{ mm}^2$. All BIB cross-sections were prepared perpendicular to the bedding of the samples and afterwards coated with a thin layer of gold, to prevent charging of the sample surfaces during SEM imaging.

SEM imaging, image processing and porosity analysis (segmentation) within representative elementary areas (REAs)

A ZEISS-supra 55 scanning electron microscope, equipped with a SE2, SE in-lens and BSE detector, as well as an EDX unit is used to image sample microstructures. The SE in-lens detector is located inside the electron column of the microscope and secondary electrons are collected with increased efficiency, but the conventional SE detector (SE2) is more suitable to image sample surface topography and morphology and therefore was used for the porosity analysis in the present study. To determine mineralogical compositions of BIB cross-sections, BSE images are combined with EDX maps, as well as EDX point analysis.

To investigate representative elementary areas (REAs) at the resolution of pore microstructures (10 nm), mosaics of hundreds of SE2-images were produced at high magnification (30,000 \times), with an overlap of 20-30% between the single images, and stitched together afterwards using Autopano (Kolor, 2012). In addition, SE2-overviews of BIB cross-sections were taken at lower magnifications (Table 2). For mineralogical mapping, mosaics of BSE-images were taken at 6,000 \times magnification and EDX analyses were done locally, to assign chemical compositions to different grey-scale values in BSE-mosaics.

To achieve statistically significant and representative results, all samples have to be investigated within representative elementary areas (REAs). Sizes of REAs were determined using the box counting method (Kameda et al., 2006; Klaver et al., 2012; Houben et al., 2013) on mineralogical compositions in BSE-mosaics, as well as segmented porosities in SE2-images, to check the comparability of REAs based on mineralogy and porosity. A stepwise growing grid is applied to the classified BSE-images, as well as to the porosity maps and at each increasing box size, the contribution of the different mineral phases, as well as the porosity contribution to the total area analysed, are calculated within that box. This process is repeated for several different starting points within the mosaics, until the individual contributions of different mineral phases and the porosity contribution do not change anymore. This area is interpreted to be the REA with regard to mineralogical composition and porosity at the scale of observation.

Pores are detected based on pixel grey-scale value information in SE2 images; whereas the interior of a pore shows very low grey-scale values (dark pixels) in SE2 images, the sample surface is characterised by much higher grey-scale values (bright pixels; Fig. 3). The porosity segmentation is done semi-automatically, applying a combination of thresholding and sobel-edge-detection algorithms in Matlab (MATLAB, 2011; Houben et al., 2013; Fig. 4b). Possible curtaining irregularities in polished BIB surfaces (Desbois et al., 2012; Klaver et al., 2012), together with background noise in SE2 images lead to difficulties in confidently detecting and segmenting very small pores of only a few pixels size (Fig. 4b), resulting in a practical pore detection resolution (PPR) at larger pore sizes than the resolution of the SE2 detector. Further problems of porosity segmentation are (1) 'pore bridging', due to very small gaps between two opposing sides of a pore, leading to the erroneous interpretation of one pore as two (or the other way round; Figs 3 and 4a), and (2) 'shallow dipping of a pore boundary', resulting in low grey-scale gradients at the pore boundary, compared to steep dips (3) (Figs 3 and 4a). Therefore, after automatic porosity segmentation, images have to be visually inspected and cleaned manually of these artefacts. This is done using the editing functions of ArcGIS (ESRI, 2011; Fig. 4c). Segmented pores are classified according to mineralogy, as long as they contribute to intra-phase porosities. Pores at the boundaries between

Table 2. Porosity data quantified from BIB-SEM approach.

Sample (ID)	Reference used	Magnification	Pixel size (nm)	Area imaged (µm ²)	REA covered	Number of pores detected	Visible porosity (%)	Mineral phase	Number of pores detected in mineral phase	Area occupied by mineral phase (% area analysed)	Porosity within mineral phase (%)	Contribution to total porosity (%)	Contribution to area analysed (%)
ON-Mol-1-164	EZE54	30,000	10	10,445	Yes	48,563	10.4	Clay matrix	48,017	76.9	12	88.1	9.2
								Quartz	467	21.9	0.3	0.7	0.1
								Inter-aggregate	79	1.2	-	11.2	1.2
		860	340	90,912	Yes	-	2-3	-	-	-	-	-	-
ON-Mol-1-196	EZE55	30,000	10	24,031	Yes	102,638	12	Clay matrix	101,066	79	13	85.4	10.3
								Quartz	1,262	19.4	0.4	0.6	0.1
								Inter-aggregate	227	1.7	-	14	1.7
		580	505	200,401	Yes	-	3-5	-	-	-	-	-	-
		330	895	572,790	Yes	-	4-5	-	-	-	-	-	-
ON-Mol-1-168	EZE52	30,000	10	25,690	No	25,773	16.9	Clay matrix	22,855	42.6	13.2	33.3	5.6
								Quartz	1,834	39.2	0.2	0.5	0.1
								Pyrite	125	0.2	20.5	0.2	<0.1
								Mica	485	4.9	18.4	5.3	0.9
								Fossils	244	0.9	14.6	0.8	0.1
								Other minerals	-	2.1	1.3	0.2	<0.1
								Inter-aggregate	230	10.1	-	59.7	10.1
		2,000	147	423,162	Yes	9,779	15.5	Clay matrix	8,100	47.8	12.9	39.9	6.2
								Quartz	514	41.1	0.3	0.7	0.1
								Mica	413	2	2.5	0.3	0.1
								Inter-aggregate	637	9.2	-	59.1	9.2
								Fossils	39	-	-	-	-
								Pyrite	96	-	-	-	-
ON-Mol-1-253	EZE64	10,000	29	64,501	No	9,171	19.9	Clay matrix	8,330	32.7	5.3	8.7	1.7
								Quartz	793	49.2	0.2	0.4	0.1
								Inter-aggregate	48	18.1	-	90.9	18.1
		475	620	301,720	Yes	-	15-16	-	-	-	-	-	-
		250	1,169	1,074,707	Yes	-	20	-	-	-	-	-	-

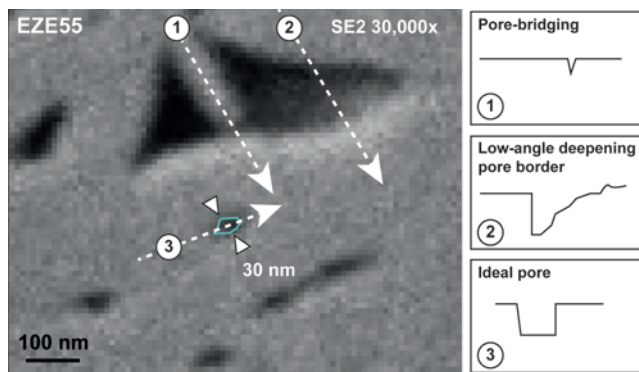


Fig. 3. SE2-micrograph of pores in Boom Clay (sample EZE55) at 30,000x magnification, illustrating typical phenomena occurring during porosity segmentation based on the difference in grey-scale values between sample surface (high grey-scale values) and pore interior (low grey-scale values): (1) 'pore bridging', due to very small gaps between sample surface material on two opposing sides of a pore, it can be difficult to identify a pore's interior as such; (2) 'low angle deepening of a pore border', due to cutting of the pore boundary by the BIB at very low angles, resulting in very small gradients in grey-scale values at the boundary, it can be hard to correctly identify the pore boundary; (3) shows an ideal pore with regard to porosity segmentation (i.e. very sharp grey-scale value differences at the pore boundary).

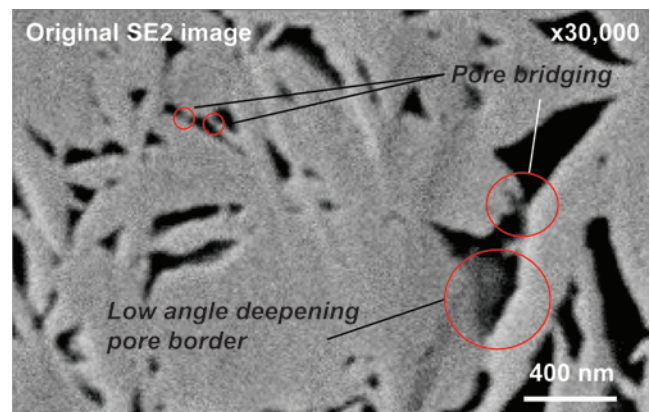
different mineral phases are referred to as inter-aggregate pores. Sizes of single pores are measured as pore areas and the orientations of the longest pore axes are calculated using the MATLAB toolbox 'PolyLX' (Lexa et al., 2005).

Terminology and limitations of the BIB-SEM method

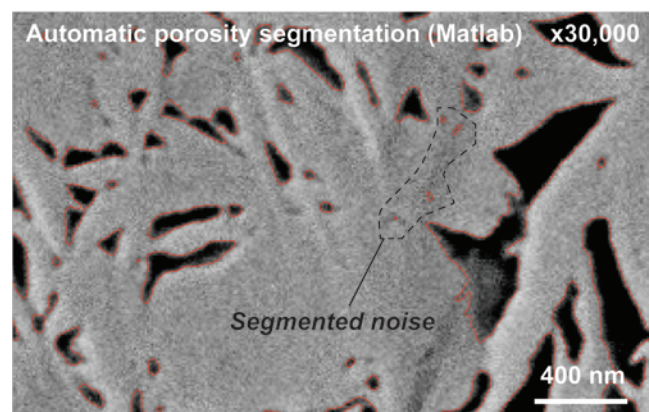
The presented method is subject to two main limiting factors: (i) sample drying and the potential creation of drying artefacts, which cannot be excluded with full confidence from the inferred microstructures and porosities (cryo-BIB-SEM investigations on water-saturated Boom Clay samples are planned in a follow-up study); and (ii) the representativeness of the obtained results. Concerning the latter, in the present study the term 'representative elementary area' (REA) refers to representativeness with regard to the scale of observation (nm- to μm -scale). However, the possibility of up scaling of the results should also be discussed. For this, MIP data obtained on cm^3 large samples are used to link our results to bulk sample properties. As will be shown, pore-size distributions measured by BIB-SEM, as well as pore-throat size distributions obtained from MIP show similar power-law exponents over several orders of magnitude, hinting towards a self-similar behaviour of the pore space in Boom Clay and indicating the possibility of up scaling of the results.

Mercury injection Porosimetry

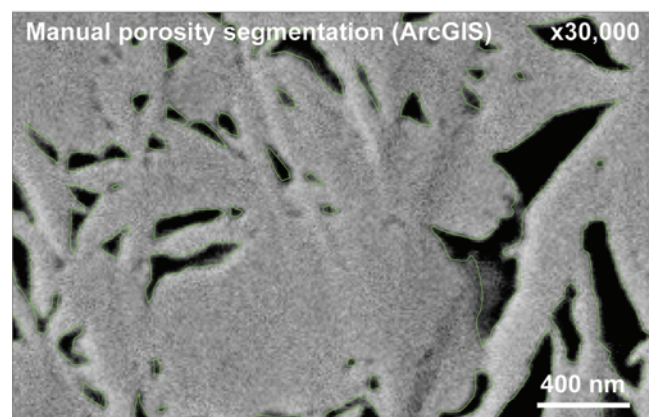
To find a link between nm-scale 2D observations and bulk sample porosities, Mercury injection Porosimetry (MIP) was carried out on the gradually oven dried samples EZE54, EZE55 and EZE64.



a.



b.



c.

Fig. 4. Illustration of semi-automatic porosity segmentation, showing a. the original SE2-image, including challenging pores ('pore bridging' and 'low angle deepening of a pore boundary' (cf. Fig. 3); in b. the same SE2-image is shown after automatic porosity segmentation (red lines), using a combination of thresholding and sobel edge detection algorithms in Matlab. Note that some background noise has also been segmented; c. depicts the same image after manual correction of the automatic results (green lines). Comparison of b and c shows that the automatic segmentation procedure gives reliable results in most cases, but some manual cleaning is necessary in case of segmentation artefacts (e.g. segmented background noise).

Washburn’s equation (Washburn, 1921; Eq. 1) describes the capillary flow through a bundle of interconnected, parallel, cylindrical tubes, and can be extended to porous media, assuming the accessible pore space to consist of interconnected, cylindrical pore tubes. The pressure (P), required to access pores of a certain size, is inversely proportional to the pore throat diameter (d):

$$P = -4 \gamma \cos \frac{\theta}{d} \tag{Eq. 1}$$

where θ is the contact angle between the Mercury and the pore walls (~139-147° for clay materials; Diamond, 1970) and γ the surface tension of the Mercury (~0.484 N/m at 25° C; Kemball, 1946; Nicholas et al., 1961). The technique measures the volume of Mercury intruding the sample at each subsequent pressure step, as the applied pressure slowly increases from ~3.6 kPa, accessing pore throat diameters ~408 μm , up to ~413 MPa, to access pores throats ~3.6 nm in diameter (in theory). During pressure drainage, extruded volumes of Mercury are measured and the difference between intrusion and extrusion curves allows deducing further information on the nature of the pore space (e.g. pore body to pore throat ratios; Webb, 2001; Cerepi et al., 2002; Janssen et al., 2011). MIP experiments were carried out using a ‘Micromeritics AutoPore IV 9500 Pore Size Analyser’ and MIP data were corrected for blank errors by Micromeritics (after Sigal, 2009). Furthermore, the samples were weighed before and after the experiment, to measure the volume of Mercury remaining inside the samples after drainage.

Power-law analysis of BIB-SEM and MIP datasets

Pore-area distributions from BIB-SEM porosity analysis

Mathematically a power-law can be described by a probability distribution function of the form:

$$p(x) = Cx^{-D} \tag{Eq. 2}$$

(Pareto, 1896-1897; Newman, 2006; Clauset et al., 2009), where $p(x)$ is the continuous probability distribution of samples with a characteristic size x , D the power-law exponent and C a constant of proportionality.

For calculation of pore-area size distributions a non-linear binning (always doubling the subsequent bin size) was used (Adamic & Huberman, 2002; Klaver et al. 2012; Houben et al., 2013), resulting in pore-size frequencies (N_i) per bin of the size (b_i). For comparison of pore-size distributions in different mosaics and samples, pore-size frequencies (N_i) were normalised by the bin size (b_i), as well as the size of the total mosaic area analysed (S_{mosaic}) and afterwards plotted against the bin-centres (S_{pore}) on a double logarithmic scale, resulting in linear distributions over several orders of magnitude (Fig. 13, left side), which could be fitted within the range of practical pore

resolution (PPR) up to the largest pores measured within the clay matrix, using least square linear regression analysis:

$$\log\left(\frac{N_i}{b_i S_{\text{mosaic}}}\right) = -D \log(S_{\text{pore}}) + \log(C) \tag{Eq. 3}$$

Taking the inverse of the logarithm on both sides, results in:

$$\frac{N_i}{b_i S_{\text{mosaic}}} = CS_{\text{pore}}^{-D} \tag{Eq. 4}$$

where D is the power-law exponent of the pore-size distribution and C a constant of proportionality. Errors were calculated based on 95% confidence range calculation.

Cumulative distribution functions of pore areas from BIB-SEM data

Commonly used methods for analysing power-law distributions, such as least-square linear regression analysis, can produce substantially inaccurate estimates of the power-law parameters (Newman, 2006; Clauset et al., 2009) and much research has been conducted on how to better describe power-law distributions. One of the most promising outcomes is to use the complementary cumulative distribution function (CCD) of a power-law distribution:

$$\Pr(X \geq x) = C \int_x^\infty p(X) dX = \frac{\alpha-1}{x_{\text{min}}^{-\alpha+1}} \int_x^\infty X^{-\alpha} dX = \left(\frac{x}{x_{\text{min}}}\right)^{-\alpha+1} \tag{Eq. 5}$$

where $\Pr(X \geq x)$ is the cumulative probability to find a pore with an area larger than or equal to x , α is the power-law exponent and x_{min} the characteristic pore size above which the data follow a hypothesised power-law distribution. This method is described in detail in Goldstein et al. (2004), Newman (2006) and Clauset et al. (2009). We used this approach to check the validity of the power-law functions derived using least square linear regression analysis.

Pore-throat-area distributions from MIP datasets

To compare MIP pore-throat distributions to BIB-SEM data, raw MIP data were converted into frequencies of pore-throat areas of a certain size (N_i^*), by dividing the intruded incremental porosity volumes per pressure step by the size of the corresponding pore-throat diameter equivalent areas. Frequencies of pore throats of a certain size (N_i^*) were normalised by the bin size (b_i) and the total volume of Mercury intruded (V_{total}). The same binning as for the BIB-SEM data analysis was used (section 2.4.1; Klaver et al., 2012; Houben et al., 2013) and for power-law analysis, the normalised frequencies ($N_i^*/b_i V_{\text{total}}$) were plotted against the bin-centres (s_{pore}^*) on a double logarithmic scale:

$$\log\left(\frac{N_i^*}{b_i V_{\text{total}}}\right) = -D^* \log(s_{\text{pore}}^*) + \log(C^*) \tag{Eq. 6}$$

taking the logarithm of both sides, results in:

$$\frac{N_i^*}{b_i V_{\text{total}}} = C^* S_{\text{pore}}^{*-D^*} \quad \text{Eq. 7}$$

D^* , the power-law exponents, and C^* , the constants of proportionality, were again inferred using least square linear regression analysis (cf. section 2.4.1; Fig. 15c) and errors calculated based on the 95 % confidence range calculation.

Estimation of changes in the porosity regime from MIP data

The Friesen-Mikula approach (Friesen & Mikula, 1987; Eq. 8) combines the 'Menger-sponge fragmentation model' (Mandelbrot, 1982; Turcotte, 1997) and Washburn's equation (Washburn, 1921; Eq. 1) to infer critical changes in the Mercury intrusion volume per pressure change, indicating possible changes in the porosity regime (Romero & Simms, 2008).

$$\frac{dV}{dp} \propto p^{D_s-4} \quad \text{Eq. 8}$$

is the first derivative of the intruded pore volume (V), with respect to the Mercury intrusion pressure (p) and can be used to calculate the surface fractal dimension (D_s) of the accessible solid – pore interface. Alternatively, taking the logarithm of Eq. 8 and normalising the intruded pore volume by the total intruded volume of Mercury (V_{total}), gives:

$$\log\left(\frac{d(V/V_{\text{total}})}{dp}\right) \sim (D_s - 4)\log(p) \quad \text{Eq. 9}$$

(after Korvin, 1992; Meyer et al., 1994 and Fadeev et al., 1996). Significant changes in D_s indicate changes in the porosity regime, or intrinsic changes in the pore network architecture. By definition, the surface fractal dimension D_s of the solid – pore interface ranges between two and three (Friesen & Mikula, 1987; Bartoli et al., 1999).

Results

Sample drying

Oven drying of samples results in total weight losses and thus water contents of 18–20 wt.-% of the original wet sample weights and corresponding water content porosities between 36–39 Vol.-%. Typical values of shrinkage strain, perpendicular to the bedding, are ~3%.

Porosity segmentation, resolution and minimum pore sizes

Keeping in mind the discussion in 2.2.2, a 'practical pore detection resolution' (PPR) was defined as the pore size above which we assume to detect close to 100% of the pores, existing of the

respective sizes. The PPR depends on the magnification used and in the present study was found at pore sizes of ~1,000 nm² at a magnification of 30,000×, and ~8,500 nm² at a magnification of 10,000×, both times corresponding to pore areas of ~10 pixel. Comparison of the results from manual and automatic porosity segmentations (Fig. 4b-c) shows a very good agreement of the results, indicating that the less time-consuming automatic porosity segmentation can be used without a critical loss of information or accuracy, as long as the automatic results are manually checked afterwards and cleaned of automatic segmentation artefacts, if necessary.

Determination of representative elementary areas (REAs)

Analyses of mineralogical compositions inferred from BSE images and EDX maps show three different mineral phases in significant amounts in samples EZE54, EZE55 and EZE64: the clay matrix, quartz and feldspar grains, and five in sample EZE52: the clay matrix, mica sheets, framboidal pyrite aggregates and quartz and feldspar grains. Other mineralogical phases, such as titanium oxide, organic matter or fossils were found only in minor amounts and therefore not included in the determination of REAs based on mineralogy. REA calculations based on mineralogy (M) in BSE images taken at 6,000× magnification and porosity (P) in SE2 images, taken at different magnifications, as indicated in Fig. 5, give the following results: REA = 64 × 64 μm (M) and 61 × 61 μm (P) at 30,000× magnification for sample EZE54 (Fig. 5a-b); REA = 94 × 94 μm (M) and 90 × 90 μm (P) at 30,000× magnification for sample EZE55 (Fig. 5c-d); REA = 287 × 287 μm (M) and 125 × 125 μm (P) at 30,000× magnification, and 295 × 295 μm (P) at 2,000× magnification for sample EZE52 (Fig. 5e-g); and REA = 453 × 453 μm (M), 153 × 153 μm (P) at 10,000× magnification, and 250 × 250 μm (P) at 475× magnification for the most coarse-grained sample EZE64 (Fig. 5h-j). The results show a very good agreement of REA calculations based on mineralogy and porosity for the two fine-grained samples (EZE54 and EZE55), whereas for the more coarse-grained samples (EZE52 and EZE64) exists a discrepancy between sizes of REAs calculated based on mineralogy and porosity at 30,000× (EZE52) and at 10,000× magnification (EZE64), respectively. For these two samples, REA calculations based on porosity were repeated at lower magnifications (2,000× for sample EZE52 and 475× for sample EZE64), to be able to cover larger areas and yield a good agreement between REA calculations based on mineralogy and porosity. This was achieved for sample EZE52, but not for sample EZE64. In the course of the present BIB-SEM study, REAs could be covered during high resolution porosity investigations at 30,000× magnification for samples EZE54 and EZE55, but not for samples EZE52 and EZE64, because of the limits of BIB polished areas.

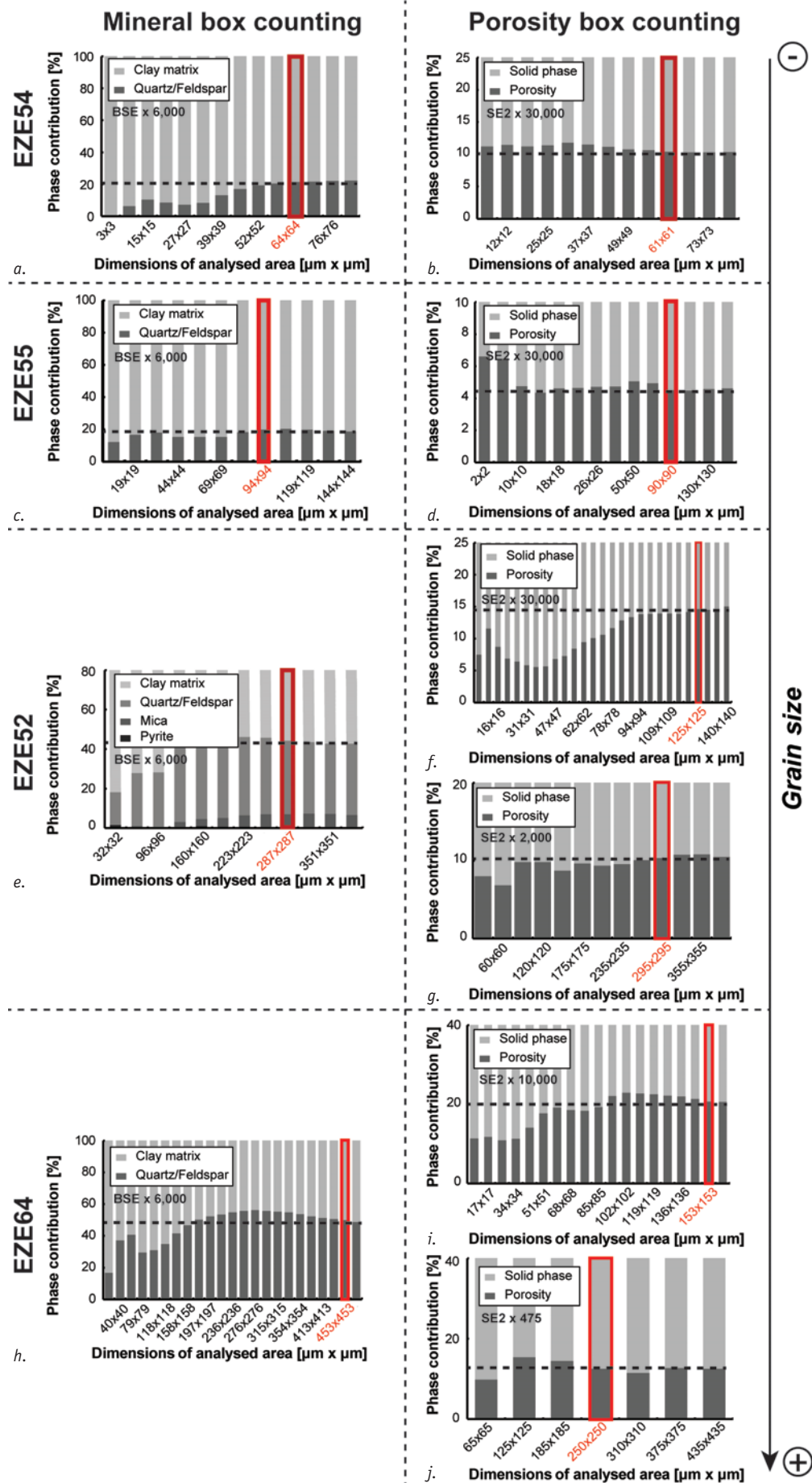


Fig. 5. Results of representative elementary area (REA) calculations based on mineralogy box-counting (left side) and porosity box-counting (right side). The graphs show the evolution of the contribution of different mineral phases, as well as porosity (%), to the whole image area analysed, with increasing box-size. The conditions of REA are fulfilled, once the contributions of mineralogical phases and porosity remain constant with increasing box size (as indicated by red frames).

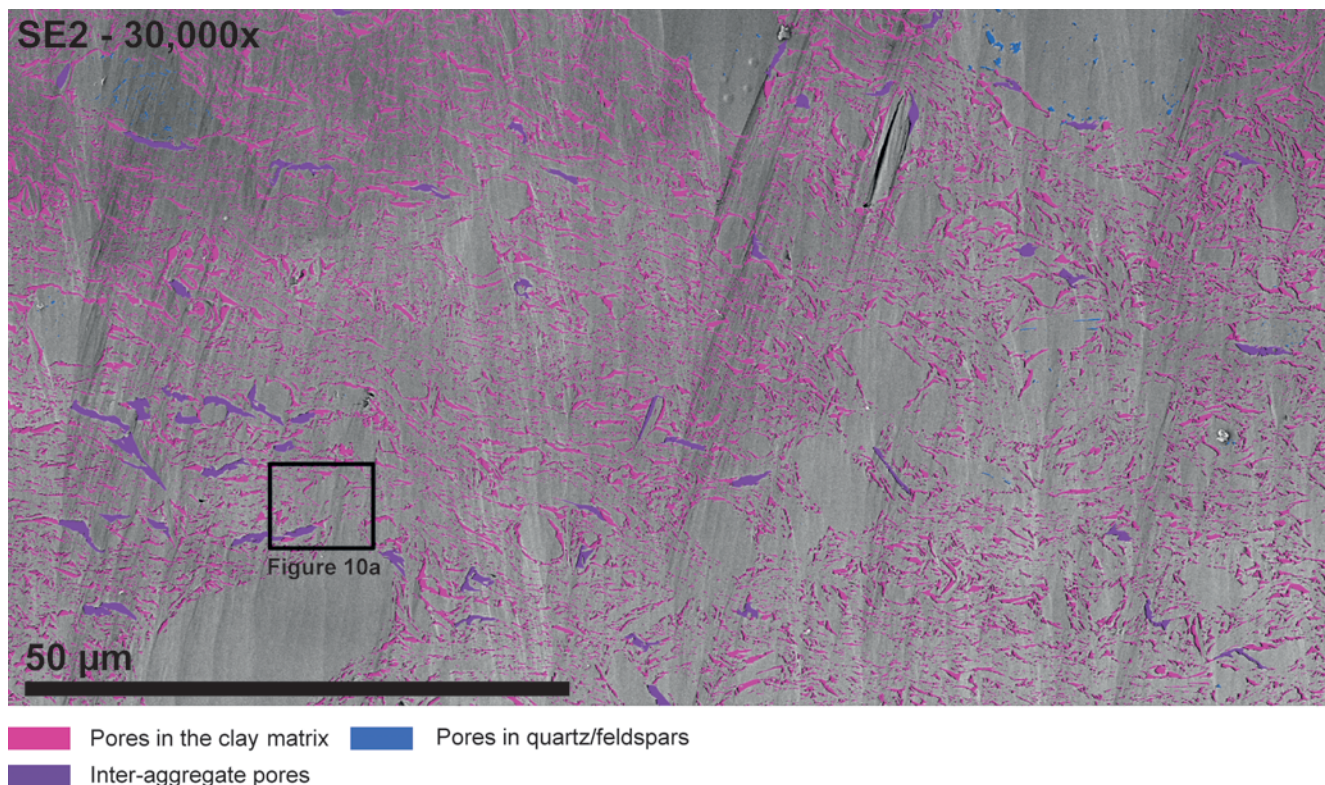


Fig. 6. SE2 microstructural overview of sample EZE54 (most fine-grained), at 30,000 \times magnification.

Porosity from BIB-SEM observations

Qualitative description of microstructures, fabrics and pore morphologies

For all samples investigated the overall microstructure can be described as a fine-grained clay matrix, embedding larger non-clay mineral grains (Figs 6-9). An increase in sample grain size is related to a decrease in clay matrix content and an increase in average pore size. In detail, the fine-grained, clay-rich samples (EZE54 and EZE55; Figs 6 and 7) show a dominance of the clay matrix, containing mainly small pores ($<1 \cdot 10^6 \text{ nm}^2$ pore area), limited by the clay-aggregate size, and very few larger non-clay mineral grains (up to 15 μm in grain diameter), which occasionally locate larger pores of up to $4 \cdot 10^6 \text{ nm}^2$ pore area in sample EZE54 (Fig. 6) and $\sim 9 \cdot 10^6 \text{ nm}^2$ pore area in sample EZE55 (Fig. 7). The coarser grained samples (EZE52 and EZE64; Figs 8 and 9) on the contrary, show a microstructure dominated by larger (up to 50 μm in diameter) non-clay minerals (mostly quartz) and a much lower clay content in between the clasts. Moreover, a higher amount of inter-aggregate pores, with characteristic sizes up to $3 \cdot 10^8 \text{ nm}^2$ in sample EZE52 (Fig. 8), and $3 \cdot 10^9 \text{ nm}^2$ in sample EZE64 (Fig. 9), was observed. The size of the largest pores, predominantly located at the boundaries between clay matrix and non-clay mineral grains, seems to increase with sample grain size.

In the present study, we distinguished the following mineral phases, which all show characteristic mineral phase internal

porosities and pore morphologies, similar in all samples investigated, irrespective of the sample depth of origin, mineralogical composition and grain-size distribution: (1) a highly porous clay matrix (Fig. 11a); (2) porous framboidal pyrite aggregates (Fig. 11b); (3) detrital mica, exhibiting porosity in between the mica sheets (Fig. 11c); and (4) non- or low-porous mineral phases, such as quartz and feldspar (Fig. 11d-f, h). Pores in the clay matrix show three different pore types (after Desbois et al., 2009): type I, elongated between similarly oriented sheet of clay (Fig. 11a, c, f); type II, crescent-shaped in saddle reefs of folded clay sheets (Fig. 11a, d, f), and type III, large jagged pores in the strain shadows of clasts (Fig. 11a, c, d and f). Typical pore sizes in the clay matrix range between several hundred nm^2 for type I pores and $\sim 1 \cdot 10^6 \text{ nm}^2$ for type III pores. In addition, there exists a large number of pores, located at the boundaries between clay matrix and non-clay mineral grains, with typical sizes $>1 \cdot 10^6 \text{ nm}^2$ in the fine-grained samples (Figs 6, 7 and 11b, d) and up to $1 \cdot 10^8 \text{ nm}^2$ in the coarse-grained samples (Figs 8, 9, 11g, h), which do not match the criteria of type I-III pores in clay. These pores were defined as 'inter-aggregate pores'. They show smooth pore edges, rounded pore tip ends and are not oriented parallel to the bedding of the samples. Furthermore, even larger pores of up to $1 \cdot 10^9 \text{ nm}^2$ pore area were observed in sample EZE64, showing smooth, rounded pore edges, bounded by, at the resolution of the SEM non-porous, homogeneous coatings (Figs 9, 11e and 12a, b), which according to EDX analysis, consist mainly of silicon, aluminium and oxygen, thus pointing towards a kaolinitic composition. These pores are not

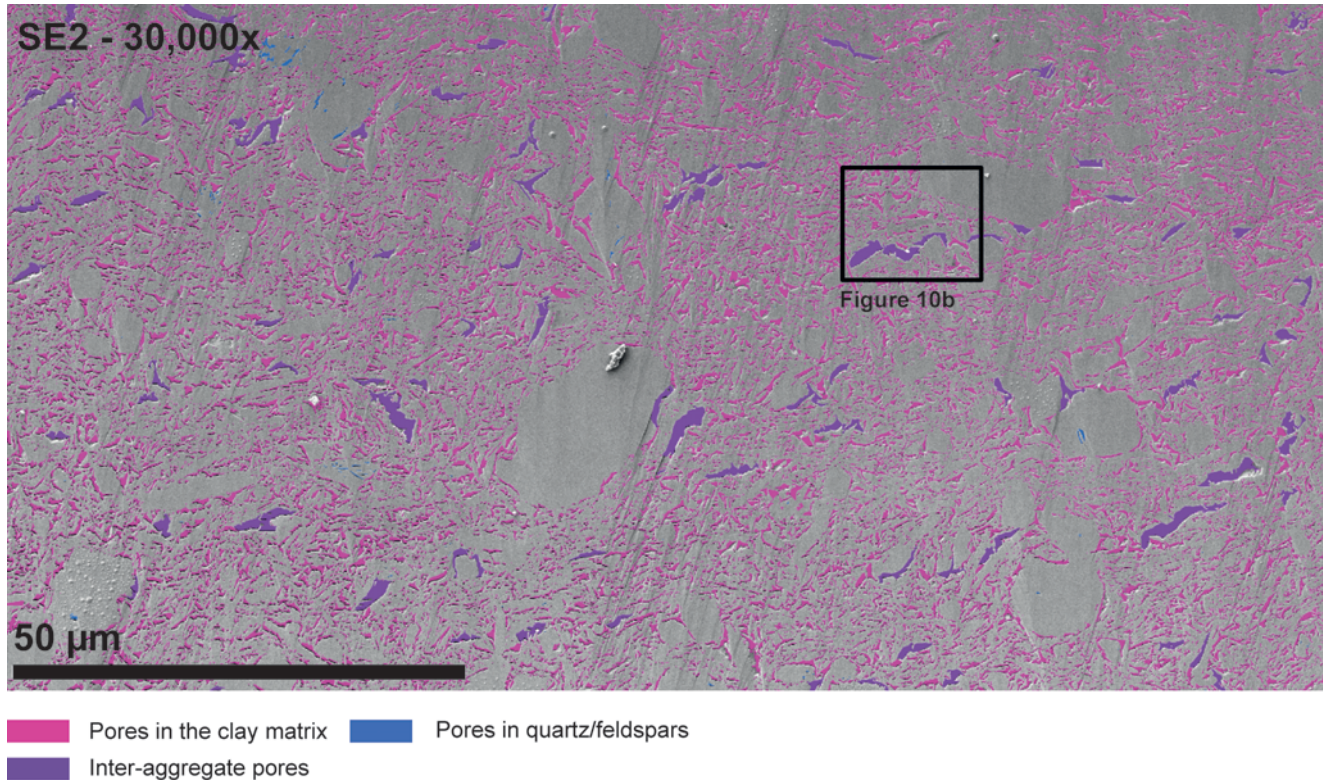


Fig. 7. SE2 microstructural overview of sample EZE55 (fine-grained), at 30,000× magnification.

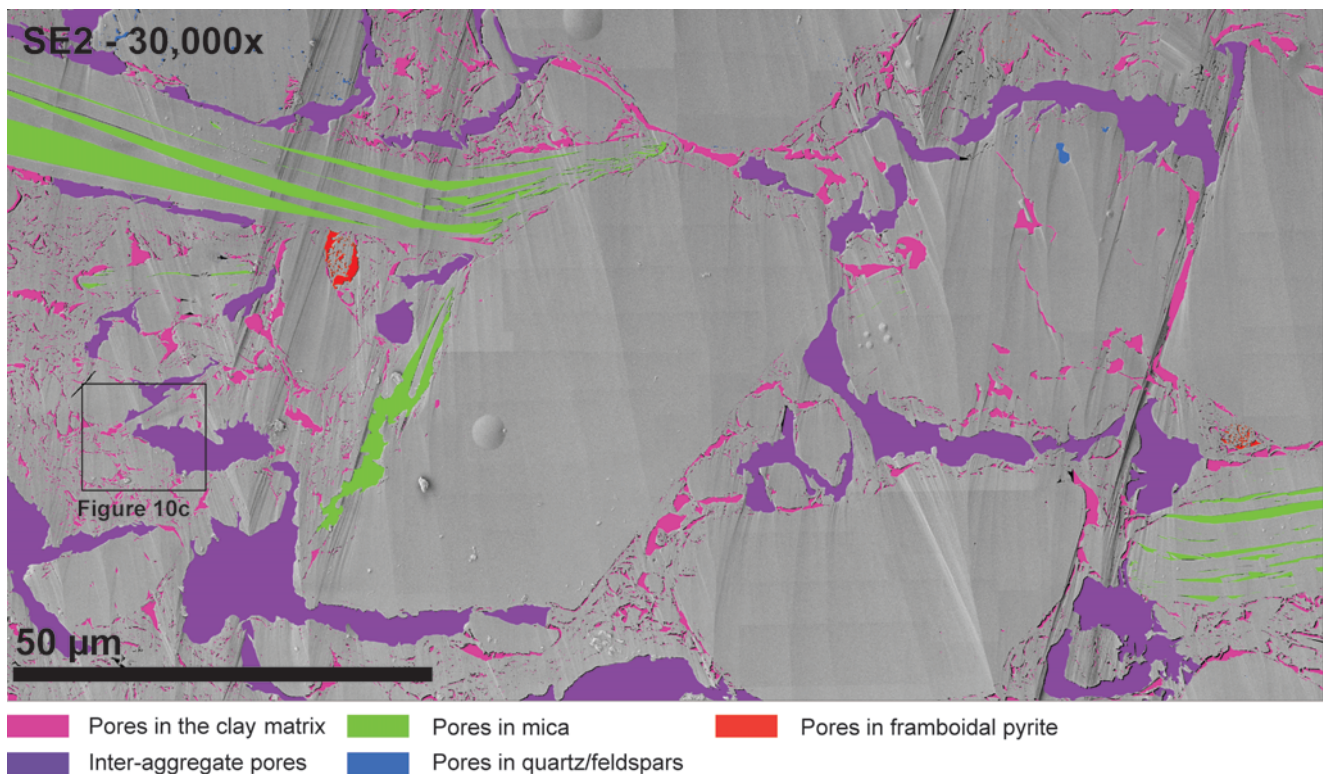


Fig. 8. SE2 microstructural overview of sample EZE52 (coarse-grained), at 30,000× magnification.

oriented along the bedding and can appear connected in 2D cross-sections, due to the 3D appearance of SEM-images in the case of larger pores (insight into the pore body over several μm; Figs 9, 11e and 12b).

Pores in pyrite framboids show characteristic serrated edges and typical sizes below $1 \cdot 10^5 \text{ nm}^2$ pore area, corresponding to the free space in between single pyrite grains (Fig. 11b). Depending on the packing of the pyrite grains, these pores can be connected

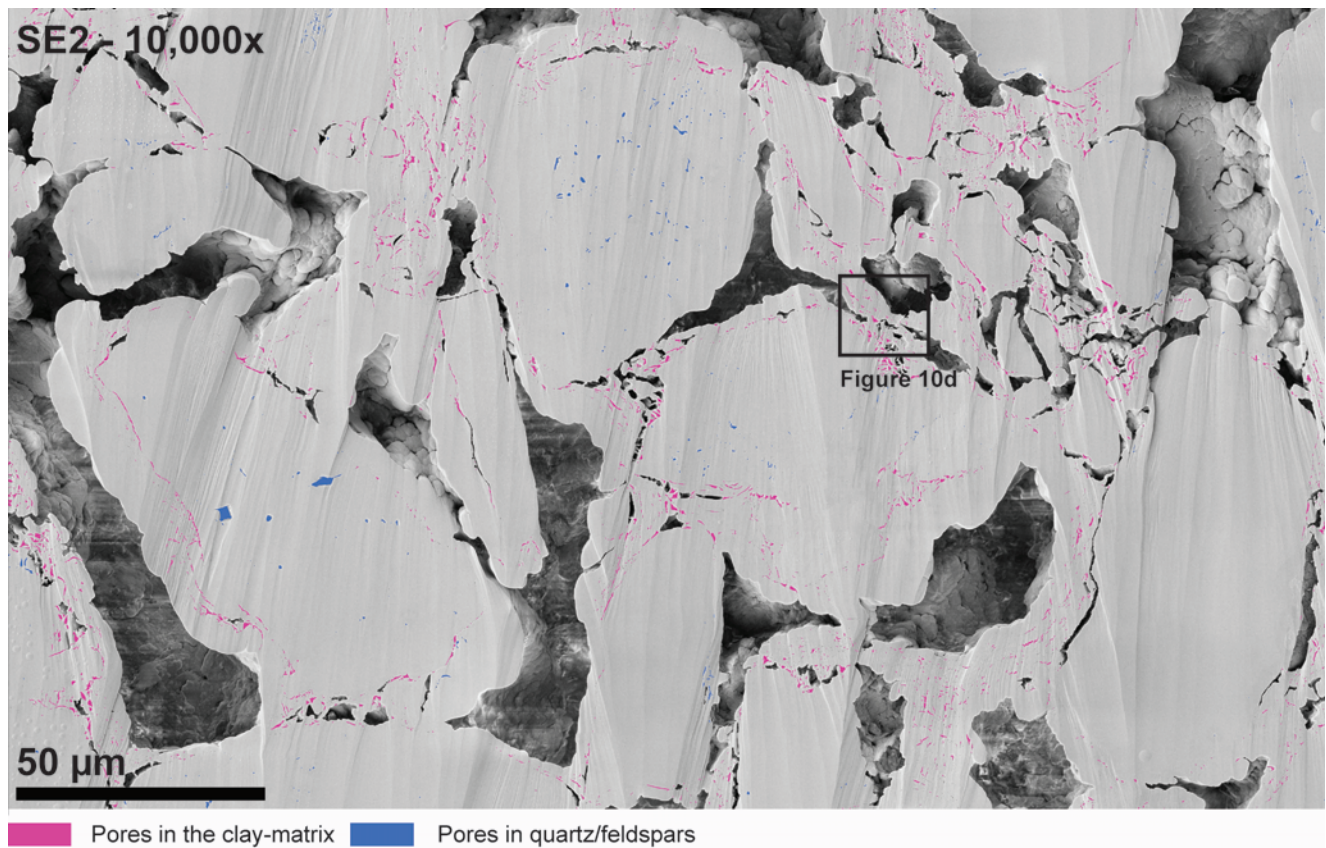


Fig. 9. SE2 microstructural overview of sample EZE64 (most coarse-grained), at 10,000× magnification.

in 2D cross-sections, occasionally as well to the surrounding clay matrix.

Pores between mica-sheets are elongated with very high aspect ratios and typical sizes $\sim 1,000 \text{ nm}^2$ in the fine-grained samples (Fig. 11c), to larger than $1 \cdot 10^8 \text{ nm}^2$ in sample EZE52 (Fig. 8). Pores in the non- or low-porous mineral phases (quartz, feldspar and titanium oxide; Fig. 11d-h) are often isometric, usually isolated and show typical sizes between 100 to $1 \cdot 10^6 \text{ nm}^2$ pore area.

Quantification of porosity from BIB-SEM investigations

Total visible porosities within REAs depend on the magnification used and range between 2-5% at very low resolutions (330-860× magnification) in the two fine-grained samples (EZE54 and EZE55) and 20% in the most coarse-grained sample (EZE64) at a magnification of 10,000× (Table 2). At identical magnification (30,000×), the results of the present study suggest a positive correlation between sample grain size and BIB-SEM visible porosity. However, for the two fine-grained samples there is a large discrepancy between total visible porosities at low (330-860×) and at high (30,000×) magnification, whereas for the two coarse-grained samples, this difference is much less pronounced (Table 2), suggesting that in the fine-grained, clay-rich samples, the overall porosity is mainly borne by small pores inside the clay matrix, whereas in the coarser grained

samples, larger pores visible at lower SEM magnifications, contribute to a more significant part of the total visible porosity. The use of high magnification ($\geq 30,000\times$) is therefore suggested to characterise the porosity in the fine-grained samples.

Pore counting indicates that most of the pores are found inside the clay matrix in all samples investigated. In the fine-grained samples (EZE54 and EZE55), pores within the clay matrix account for 85-88% of the total BIB-SEM visible porosity at 30,000× magnification, whereas in the coarser grained sample EZE52, pores in the clay matrix contribute to only 33% of the total visible porosity at the same magnification, and to $\sim 40\%$ at 2,000× magnification. In the most coarse-grained sample (EZE64) only $\sim 9\%$ of the total visible porosity at 10,000× magnification is observed in the clay matrix. Inter-aggregate pores account for the majority of the porosity in this sample ($\sim 91\%$), as well as in sample EZE52 ($\sim 60\%$), whereas in the two fine-grained samples, these pores contribute to only 11 (EZE54) and 14% (EZE55) of the total BIB-SEM visible porosity. Porosity in other than clay mineral phases (quartz, feldspar, mica, pyrite, fossils and titanium oxide) contributes to a less significant amount to the total detected porosities (Table 2), but it is interesting to note that at the same magnification (30,000×), the porosity detected in the clay matrix and in quartz seems to be consistent for all samples investigated (Table 2).

Statistical analysis of the pore-area sizes measured within the clay matrix (type I, II and III pores) shows log-normal

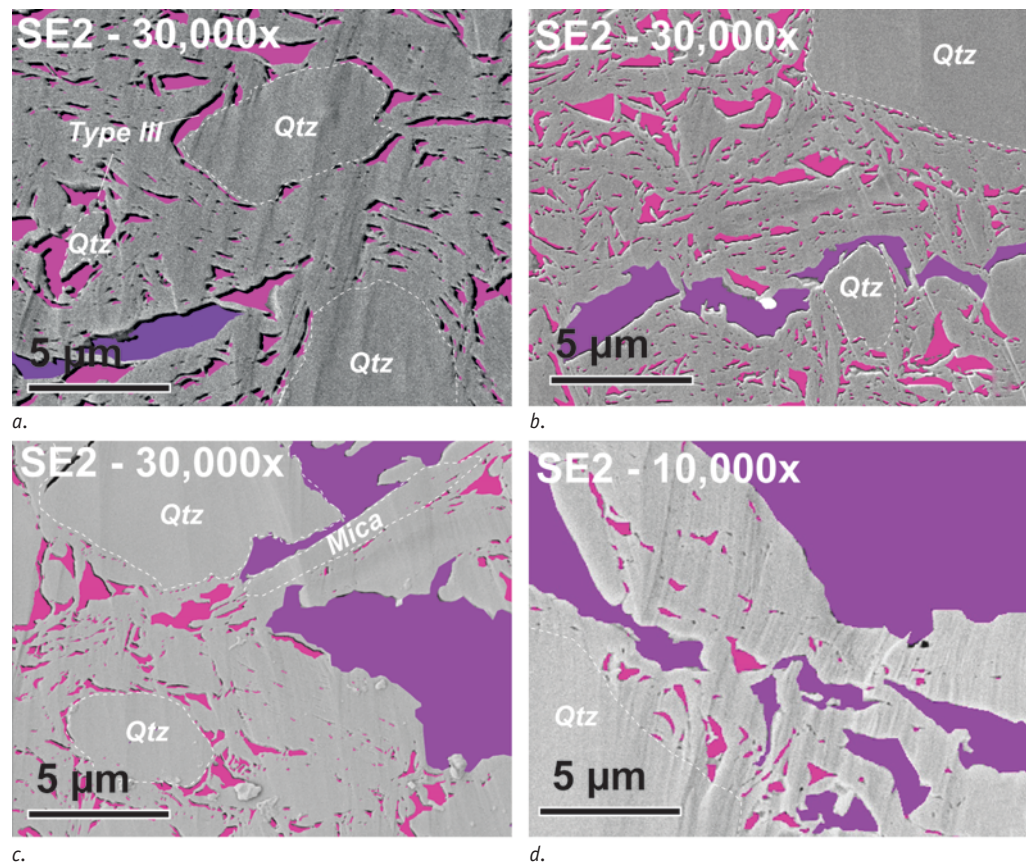


Fig. 10. Details of segmented porosities within the clay matrix of samples EZE54 (a), EZE55 (b) and EZE52 (c), analysed at 30,000 \times magnification, as well as sample EZE64 (d), investigated at 10,000 \times magnification, showing similar characteristic porosities and pore morphologies within the clay matrix, for all samples investigated.

distributions with peaks $\sim 1,000 \text{ nm}^2$ pore area for samples EZE54, EZE55 and EZE52 (30,000 \times magnification), and $\sim 8,500 \text{ nm}^2$ for sample EZE64 (10,000 \times magnification), which coincides with the practical pore detection resolutions (PPRs) at the respective magnifications. Below the PPR, down to the resolution of the SEM ($\sim 100 \text{ nm}^2$ at 30,000 \times and 850 nm^2 at 10,000 \times magnification), some pores could still be interpreted in the SE2 images, but these do not represent all the pores of the respective sizes, as explained before). Therefore, pores below the PPR were not taken into account during the quantitative analysis of pore-size distributions.

Plotting normalised frequencies of measured pore areas as a function of pore size on a double logarithmic scale (Fig. 13a, c, e, g), we observe linear pore-area distributions over 3–4 orders of magnitude, between the PPR and the largest pores detected within the clay matrix, indicating a power-law behaviour of pore sizes within the clay matrix. Least-square linear regression analysis of the linear sections gives power-law exponents between 1.56–1.66. In detail, the received power-law parameters are: $D = 1.63 \pm 0.16$, $\text{Log}(C) = -3.63 \pm 0.75$ for sample EZE54 (Fig. 13a); $D = 1.56 \pm 0.17$, $\text{Log}(C) = -3.92 \pm 0.78$ for sample EZE55 (Fig. 13c); $D = 1.64 \pm 0.07$, $\text{Log}(C) = -4.31 \pm 0.35$ for sample EZE52 (Fig. 13e), and $D = 1.66 \pm 0.07$, $\text{Log}(C) = -4.55 \pm 0.4$ for sample EZE64 (Fig. 13g). The power-law exponents of pore-area size distributions within the clay matrix are similar for all samples investigated, regardless of the depth of origin, mineralogical composition or grain-size distribution of the sample.

The complementary cumulative probability distributions (CCDs) were calculated for the same data (Fig. 13b, d, f, h). At small pore sizes, the results substantiate our hypothesis and the CCDs of pore areas can be approximated using power-laws, with exponents between 1.66–1.74, thus only slightly higher than calculated by least square linear regression analysis. However, towards larger pore sizes ($> \sim 1 \cdot 10^5 \text{ nm}^2$ pore area for the two fine-grained samples; Fig. 13b, d; $> \sim 5 \cdot 10^5 \text{ nm}^2$ for sample EZE52, Fig. 13f, and $> \sim 2 \cdot 10^6 \text{ nm}^2$ for sample EZE64, Fig. 13h), the complementary cumulative probability distributions deviate significantly from the hypothesised power-law behaviour.

Orientations of the longest axes of pores, segmented within the clay matrix, show a clear preferred orientation sub-parallel to the bedding in the two fine-grained samples (EZE54 and EZE55; Fig. 14a, b), a random distribution in the coarse-grained sample EZE52, investigated at 30,000 \times magnification (Fig. 14c), and two preferred orientations, one sub-parallel and one sub-perpendicular to the bedding for the same sample, analysed at 2,000 \times magnification (Fig. 14d). The most coarse-grained sample (EZE64) shows a preferred orientation of the pores longest axes sub-perpendicular to the sample bedding (Fig. 14e).

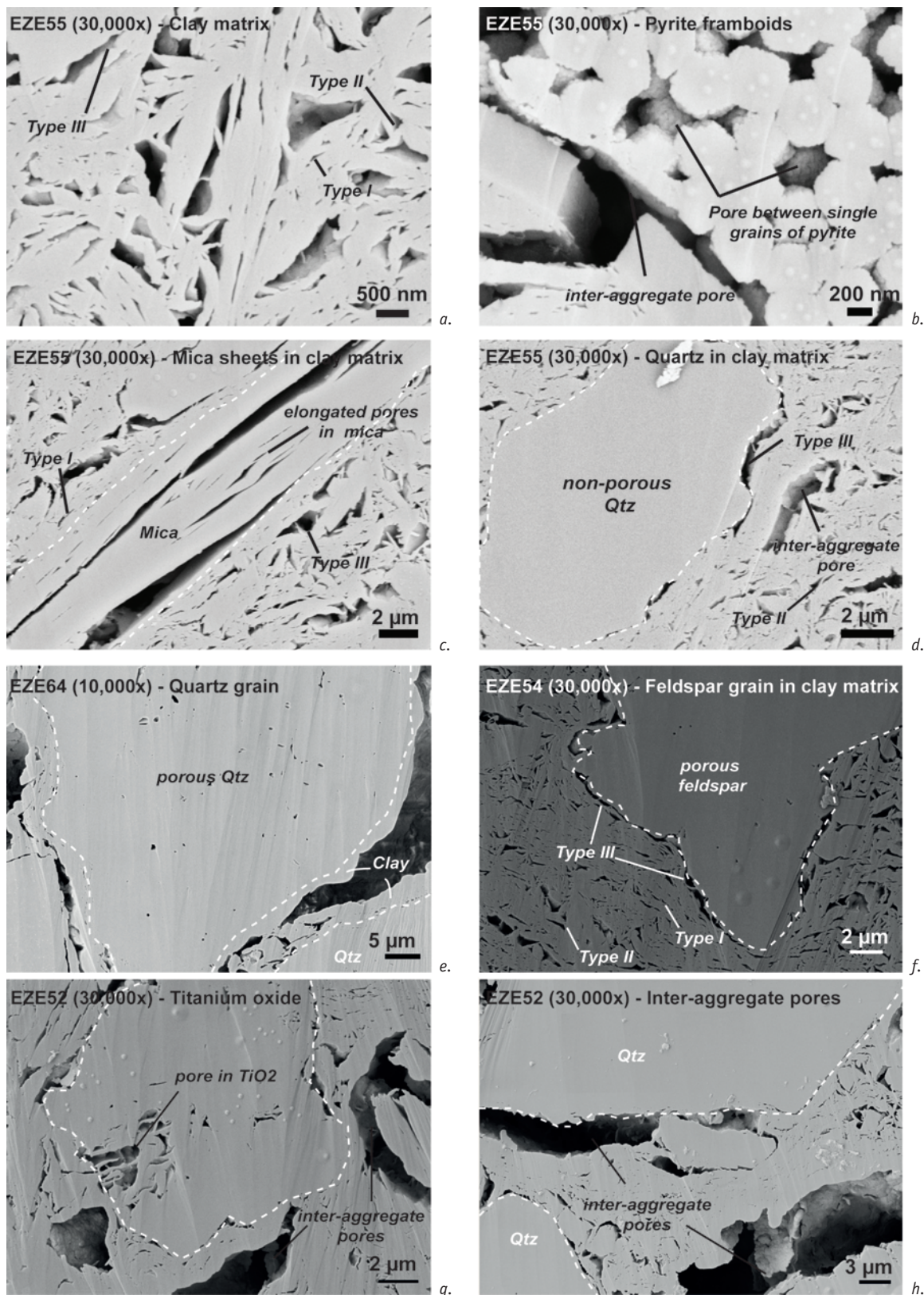


Fig. 11. Characteristic pore morphologies in different mineral phases: a. pores of type I, II and III inside the clay matrix; b. typical pores in pyrite framboids; c. pores between detrital sheet of mica; d. non-porous quartz grain, embedded in the clay-matrix, showing pores of type II and type III in the strain shadows of the quartz grain, as well as inter-aggregate pores in the clay matrix; e. porous quartz grain, coated by a very dense, probably clayey, rim; f. low-porous feldspar grain, embedded in the clay matrix and surrounded by pores of type III, in the strain shadow of the feldspar grain, as well as type I and II pores in the clay matrix; g. pores in titanium oxide and large inter-aggregate pores in the surrounding clay matrix; h. large inter-aggregate pores at the boundaries between clay matrix and non-porous quartz grains.

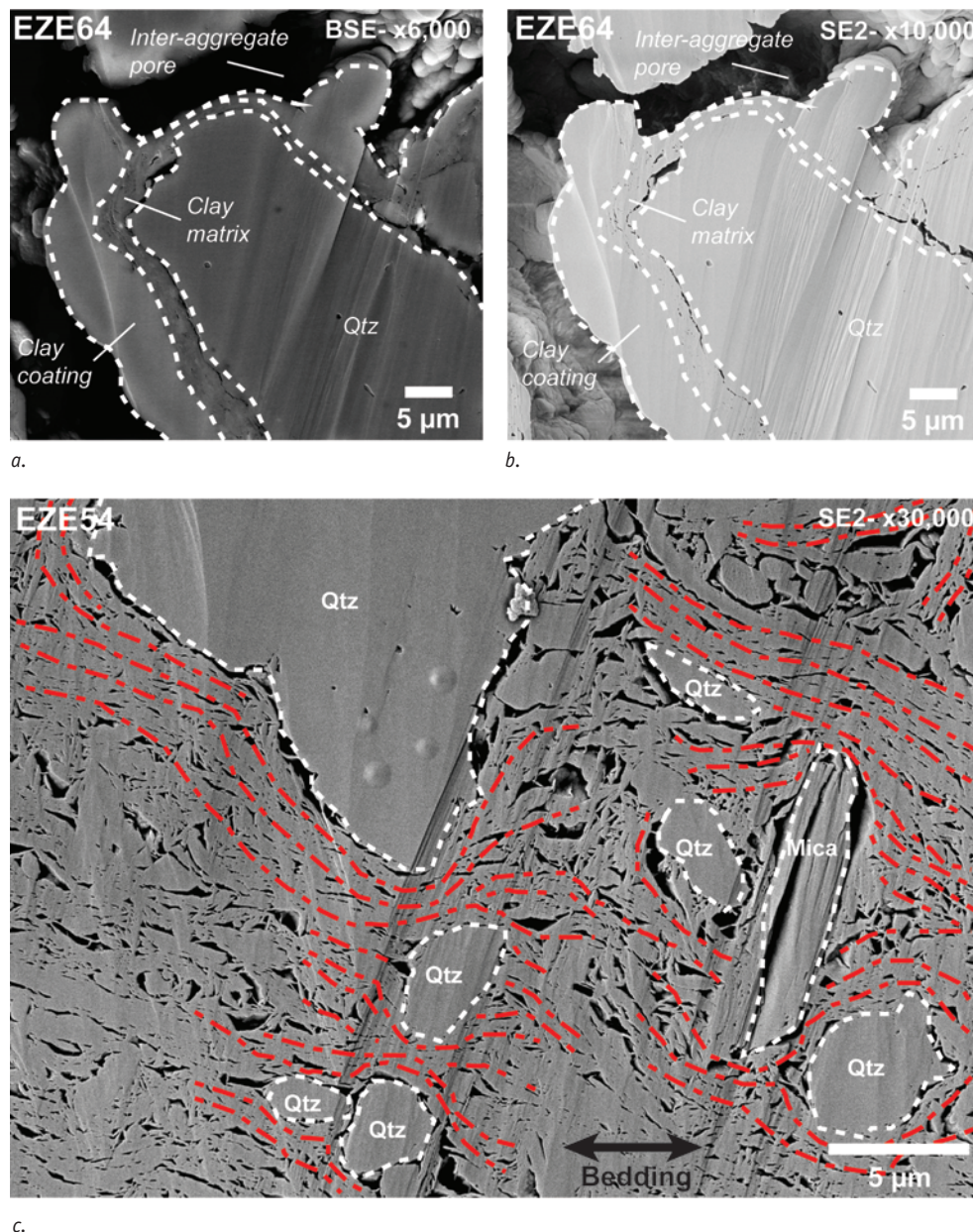


Fig. 12. *a* and *b*: close-up view of a typical, very large pore found in sample EZE64; *a*. BSE-image taken at 6,000 \times magnification; and *b*. SE2-micrograph taken at 10,000 \times magnification. Due to their smooth internal pore walls and rounded pore edges, these type of pores were also classified as inter-aggregate pores although some clear differences are discernible, compared to the usually defined inter-aggregate pores; these are, the surrounding very dense (kaolinitic) coatings on the adjacent quartz grains, as well as the much larger typical sizes of the pores; *c*. deviation of the preferred orientation (red dashed lines) from bedding-parallel (horizontal in the image) of the clay minerals and pores within the clay matrix, in the vicinity of rigid clasts (e.g. quartz, feldspar or mica).

Mercury injection Porosimetry

Correction of the original MIP data

Mercury injection Porosimetry (MIP) indicates a 3D bulk connected porosity of 27% for samples EZE54 and EZE55, and 35% for sample EZE64 (Fig. 15a). Mercury is injected into all samples at pressures corresponding to pore-throat diameters $>30\ \mu\text{m}$, even if BIB-SEM microstructural observations do not show pores of that size in the two fine-grained samples, and only very rarely in the coarse-grained sample EZE64. The Mercury data were therefore corrected by subtracting porosity volumes intruded at pore-throat diameters $>30\ \mu\text{m}$, which we interpreted as either surface roughness effects or conformance errors (Sigal, 2009; Klaver et al., 2012), or to correspond to larger cracks, possibly induced by the drying of samples.

MIP results

After surface roughness and drying artefacts correction, MIP gives total interconnected porosities of 26.4% for sample EZE54, 26.6% for sample EZE55 and 32.1% for sample EZE64 (Fig. 15a). Volume porosity distributions, plotted as a functions of pore-throat size, show unimodal distributions for samples EZE54 and EZE64 and a bi-modal distribution for sample EZE55, with major peaks found at pore-throat diameters $<100\ \text{nm}$ in the two fine-grained samples (EZE54 and EZE55) and $\sim 10,000\ \text{nm}$ in the coarse-grained sample (EZE64; Fig. 15b). Pores $<300\ \text{nm}$ pore-throat diameter contribute to $\sim 94\%$ of the total MIP volume in sample EZE54, whereas in sample EZE64, pores larger than $3,000\ \text{nm}$ pore-throat diameter account for $\sim 70\%$ of the total intruded porosity volume. For sample EZE55, pores with throat diameters smaller than $300\ \text{nm}$ contribute to $\sim 62\%$ of the total MIP volume,

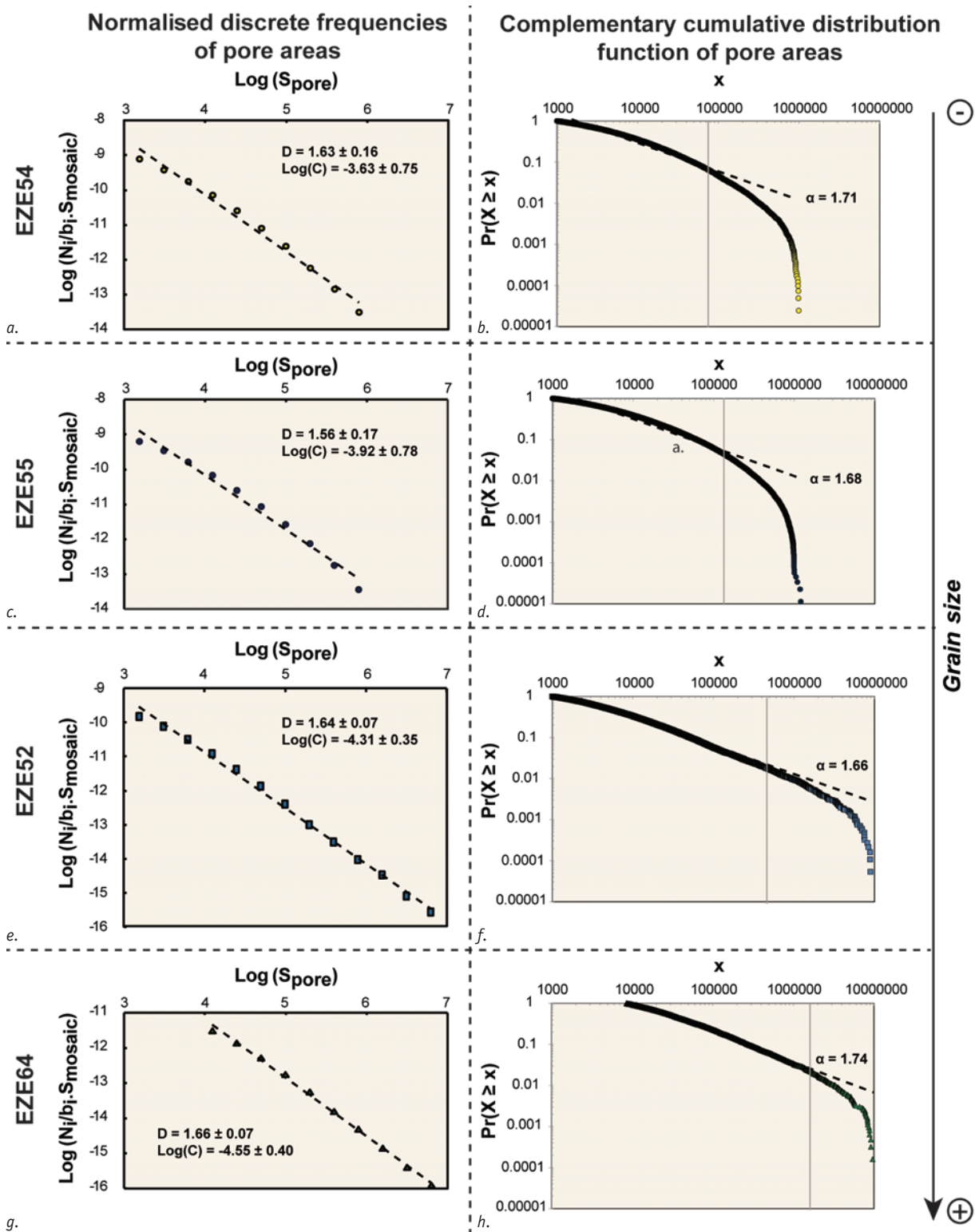


Fig. 13. Results of power-law analysis of pore-size distributions within the clay matrix. a, c, e and g show the results of least-square linear regression analysis on double logarithmic plots of normalised pore-area frequencies against the pore-size (area), using a non-linear, logarithmic binning. The results indicate a power-law distribution of pore areas, down to the practical pore resolution (PPR) $\sim 1,000 \text{ nm}^2$ in samples EZE54, EZE55 and EZE52 ($30,000\times$ magnification) and $\sim 8,500 \text{ nm}^2$ pore area in sample EZE64, analysed at $10,000\times$ SEM magnification. Plots b, d, f and h depict the complementary cumulative probability distributions (CCDs) of the same pore area data, indicating a deviation from the hypothesised power-law behaviour for pore-sizes larger than $\sim 1\cdot 10^5 \text{ nm}^2$ in samples EZE54 (b) and EZE55 (d), $> \sim 5\cdot 10^5 \text{ nm}^2$ in sample EZE52 (f) and $> \sim 2\cdot 10^6 \text{ nm}^2$ pore area in sample EZE64 (h), due to the non-representativeness of analysed areas with regard to larger pore sizes. Inferred power-law exponents (D and α) are given directly on the figures, and are similar for all samples investigated and constant over several orders of magnitude.

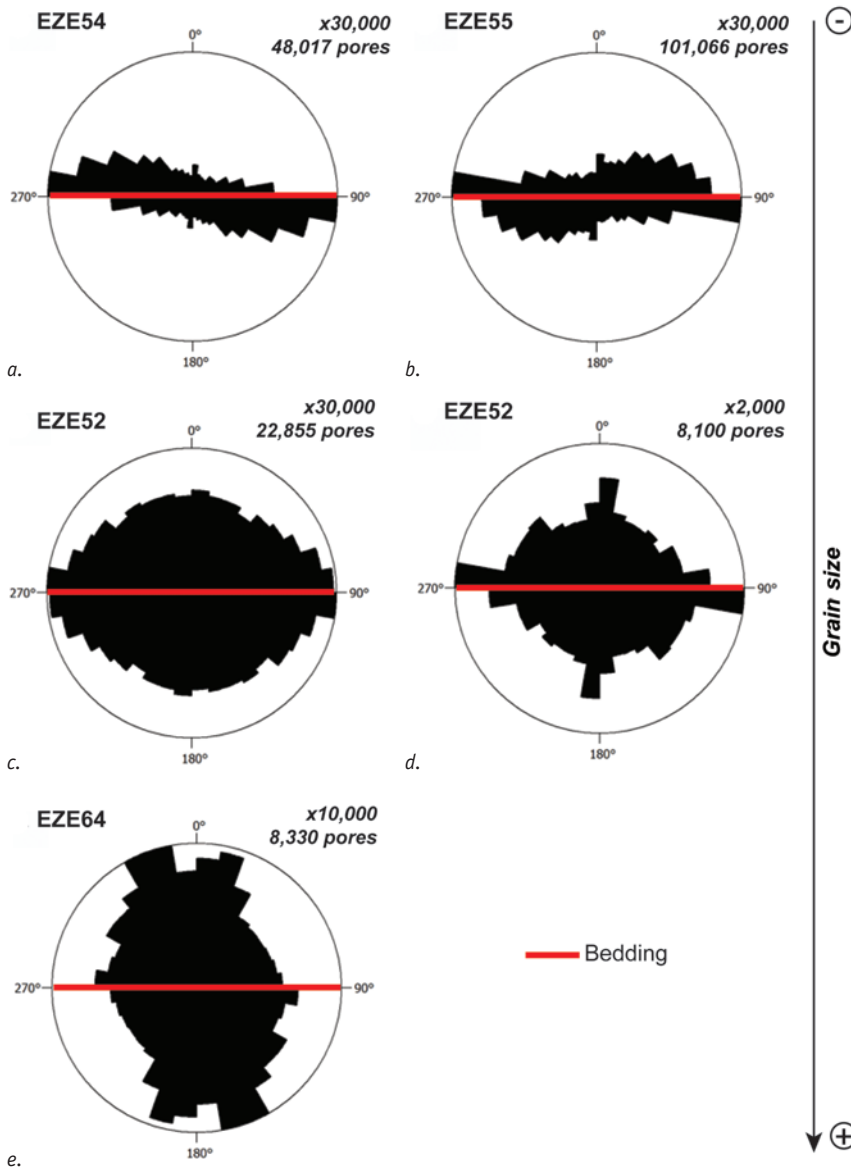


Fig. 14. Rose diagrams, indicating the (pre-dominating) orientation of the longest axes of pores, segmented within the clay matrix. A strong preferred orientation of pores sub-parallel to the bedding was found in the two fine-grained samples (EZE54 (a) and EZE55 (b)). For the coarse-grained sample EZE52, orientations of the longest axes of pores show a random distribution, from investigations carried out at 30,000× magnification (c) and two preferred orientations, one sub-parallel and one sub-perpendicular to the bedding, from porosity analysis at 2,000× magnification (d). The most coarse-grained sample (EZE64) shows a prevailing orientation of the pores longest axes, sub-perpendicular to the sample bedding (e).

and pores >3,000 nm account for ~13%. Comparison of MIP intrusion and extrusion curves shows a strong hysteresis in the data (Fig. 15a), indicating that a significant volume of Mercury remains inside the samples after drainage and hinting towards large pore-body to pore-throat ratios (Webb, 2001). Calculated pore-body to pore-throat ratios are between 1.2-50 in the two fine-grained samples (EZE54 and EZE55) and between 1.3-100 in the coarse-grained sample (EZE64), with an increasing pore-body to pore-throat ratio towards larger pore sizes. Measured residual porosities after drainage are 16.1 Vol.-% for sample EZE54, 19.1 Vol.-% for sample EZE55 and 30.1 Vol.-% for sample EZE64 (Fig. 15a; surface roughness corrected data). These porosity volumes are in good agreement with the porosities calculated from the sample weight gains after the experiment, of 14.8 Vol.-% for sample EZE54, 18 Vol.-% for sample EZE55 and 30.6 Vol.-% for sample EZE64, suggesting that the Mercury really has entered the samples and remained within after the experiment (Hildenbrand & Urai, 2003).

Power-law analysis of the MIP data

Figure 15c depicts the normalised pore-throat frequencies, measured by MIP, as a function of equivalent pore-throat-area on a double logarithmic scale, showing straight lines over ~8 orders of magnitude. Power-law exponents, resulting from least-square linear regression analysis are $D^* = 2.23 \pm 0.08$ for sample EZE54, 2.09 ± 0.05 for sample EZE55 and 1.89 ± 0.06 for sample EZE64 (Fig. 15c; errors based on 95% confidence range calculation). These power-law exponents are higher than the values obtained from power-law analysis of the BIB-SEM measured pore-area distributions (Fig. 13).

Applying the ‘Friesen-Mikula approach’ (cf. Eqs 8 and 9) and plotting normalised intruded porosity volumes ($d(V/V_{total})$) per pressure change (dp) against the absolute applied Mercury pressures (p) on a double logarithmic scale (using uncorrected data), indicates different porosity regimes based on significant changes in the intruded porosity volumes per pressure change

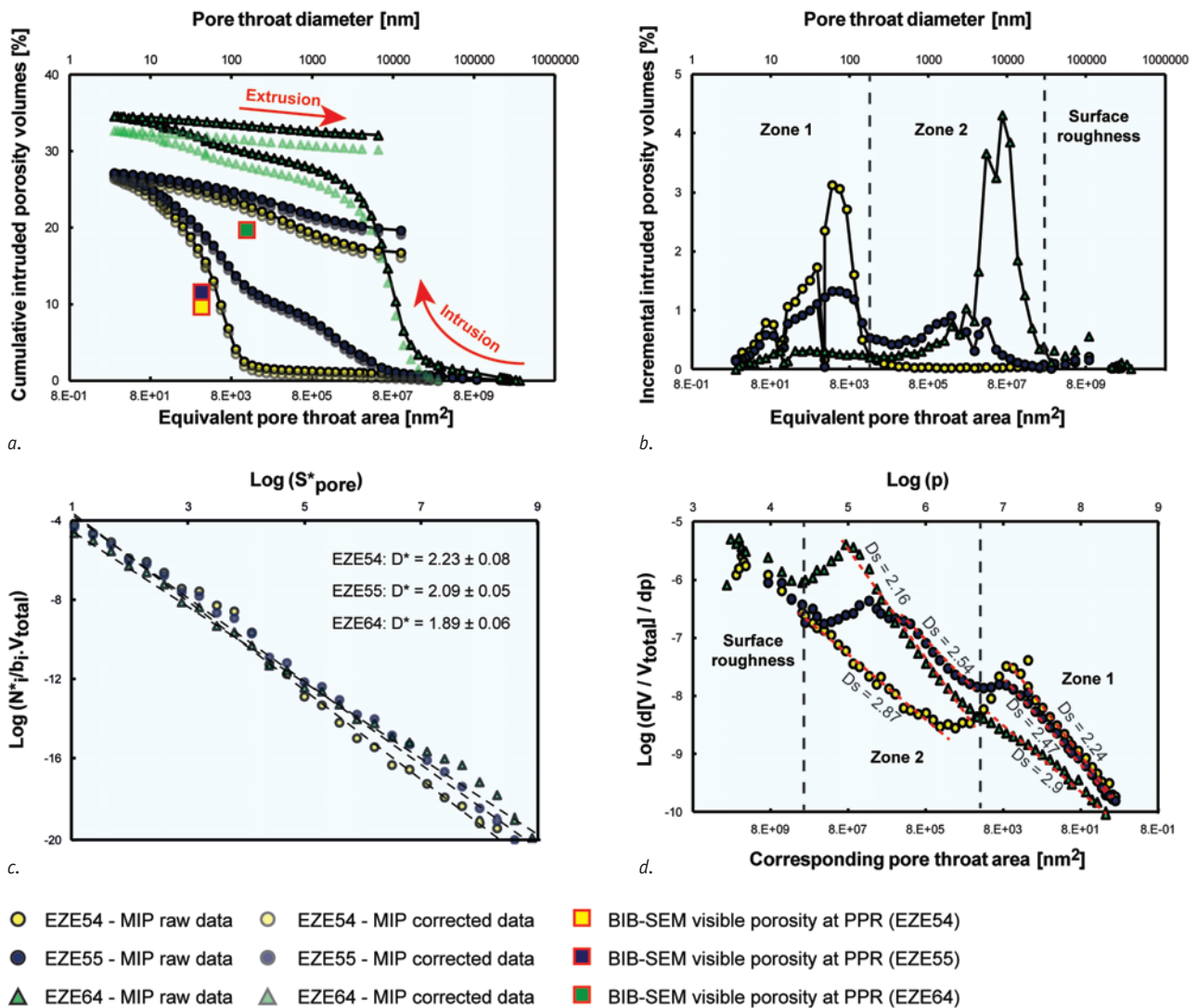


Fig. 15. Results of Mercury injection Porosimetry on samples EZE54, EZE55 and EZE64. a. Cumulative Mercury intrusion and extrusion curves, as a function of pore-throat size; full symbols indicating uncorrected data and transparent symbols, data corrected for surface roughness effects. Total BIB-SEM visible porosities at practical pore detection resolutions (PPRs) are indicated by squared symbols; b. MIP inferred porosity distributions, as a function of pore-throat size, indicating three different porosity regimes; c. log-log distributions of pore-throat frequencies vs. pore-throat size (area), using surface roughness corrected data, fitted using least-square linear regression analysis. Resulting power-law exponents (D^*) are indicated directly on the plots, together with errors, based on 95% confidence range calculation; d. changes in intruded porosity volumes ($d(V/V_{total})/dp$) per pressure change (dp), indicating different porosity regimes, plotted against the absolute applied pressure (p) on a double logarithmic scale; surface fractal dimensions (D_s) can be inferred from power-law fitting of the linear sections of the double logarithmic plots, and for zones 1 and 2 are reported directly on the plot.

(Fig. 15d). We identified two major boundary regions between different porosity regimes: the first one at pore-throat sizes $\sim 2 \cdot 10^4 \text{ nm}^2$ pore-throat area and a second one $\sim 2 \cdot 10^8 \text{ nm}^2$, interpreted as corresponding to the boundary between large pores (zone 2) and surface roughness effects. The first boundary, corresponding to the boundary between zone 1 (small pore throats) and zone 2 (large pore throats), was determined empirically from clear changes in D_s , calculated from the slopes of double logarithmic plots of changes in the intruded porosity volumes per pressure change ($d(V/V_{total})/dp$) vs the absolute applied pressure (p), using linear regression analysis (Fig. 15d). Resulting surface fractal dimensions (D_s) of the solid – pore

interfaces for the different porosity regimes are: $D_s = 2.24$ (zone 1) and 2.87 (zone 2) for sample EZE54, comparable to the results for sample EZE55 of $D_s = 2.47$ (zone 1) and 2.54 (zone 2). For sample EZE64, the transition between zone 1 and zone 2 is less pronounced, due to a much smoother change in the intruded porosity volumes per pressure change, but still two different porosity regimes, showing different surface fractal dimensions of 2.9 (zone 1) and 2.16 (zone 2), could be distinguished (Fig. 15d).

Discussion

Sample drying

Sample water contents (18–20 wt.-%), as well as inferred water content porosities (36–39 Vol.-%), measured from the weight loss of samples during drying, are in good agreement with established Boom Clay water contents (~19–24 wt.-%, e.g. De Craen et al., 2004) and water content porosities (~37% on average, e.g. Boisson, 2005). We can be sure to not having removed any interlayer, clay-bound water from the samples, since they were never heated to more than 100° C.

A significant part of the shrinkage of samples during drying (~3% along the axis perpendicular to the bedding) is interpreted to be due to volume changes of clay minerals during desiccation. In addition to the gradient of shrinkage-strain between the outside and the inside of a bulk sample, clay – non-clay mineral interfaces may possibly localise drying-induced damage of the sample microstructure, due to a non-uniform deformation of clay and non-clay mineral phases and the resulting build-up of stress at their interfaces. Therefore, we cannot fully exclude the possibility of drying artefacts at clay – non-clay mineral interfaces from our investigations. However, the morphology of most inter-aggregate pores points towards non-drying artefacts, since they show smooth, rounded edges, which is incompatible with the typical morphological features of drying artefacts (e.g. Heath et al., 2011). One way to quantify the impact of sample drying would be to compare microstructures in dried samples to those in undried, wet-preserved samples, investigated under cryogenic (BIB-SEM) conditions (Desbois et al., 2013). Another option to observe the impact of sample drying in-situ, is to dry samples inside a micro-CT scanner, during investigations. However, although part of the porosity measured in this study may be related to drying, we note that a number of studies on Boom Clay porosity has been carried out on dried samples (e.g. Al-Mukhtar et al., 1996; Boisson, 2005 and Dehandschutter et al., 2005) and the same arguments hold for the results of these.

Pore detection resolution and REAs

The practical pore resolution (PPR) depends on the magnification used during SEM imaging. The PPR was found ~1,000 nm² pore area at a magnification of 30,000× and ~8,500 nm² at a magnification of 10,000×, corresponding to the size of ~10 pixels at both magnifications, suggesting that the quality of the pore segmentation is reproducible and does not depend on the magnification used. The fact that the detection of pores below the PPR is incomplete, was interpreted to be one reason for the deviation of measured pore-area size distributions from following a power-law, at pore sizes below the PPR (Klaver et al., 2012; Houben et al., 2013). Below the PPR the detection of pores is assumed to be linked to the morphology of the pores,

with round pores, showing steep pore edges, being more easy to detect than elongated pores with high axial ratios. Additional effects, making the detection of pores more complicated, are shadowing of pores by surface roughness effects on BIB polished cross-sections, or the gold coating of the sample surfaces (Klaver et al., 2012).

Comparison of porosities measured using the BIB-SEM approach at the practical pore detection resolution and MIP at pressures corresponding to PPR (Fig. 15a), shows that BIB-SEM porosities are below the porosities measured by MIP. This brings us back to the question of whether an area large enough to be representative of bulk sample porosities can be investigated at the scale of BIB-SEM observations. For sample EZE64, the discrepancy between BIB-SEM and MIP porosities can be explained by the fact that the size of REA was not reached for this sample during BIB-SEM investigations. However, for samples EZE54 and EZE55, also a discrepancy of ~40%, similar to the difference for sample EZE64, exists between MIP and BIB-SEM measured porosities at identical resolutions. We interpret this difference to be due to larger pores or cracks, as a result of sample drying, which are omitted during BIB-SEM analysis, but most likely present in the much larger sample volumes analysed during MIP. Therefore, we conclude that areas investigated by BIB-SEM are not representative of larger pores or cracks, possibly existing on a larger scale, but still can be considered as representative of the microstructure and clay matrix controlled porosities in the two fine-grained samples (EZE54 and EZE55). On the other hand, for the two coarser grained samples (EZE52 and EZE64), larger areas would have to be investigated using BIB-SEM, to be able to cover areas representative of the samples' characteristic microstructural features and porosities, which in these samples are controlled by larger 'inter-aggregate' pores, occurring mostly at clay – non-clay mineral interfaces, rather than by clay matrix internal porosities.

Variability of pore characteristics in different samples investigated

One of the major findings of this work is that at the scale of the cross-section overviews (Figs 6–9), all samples investigated are built in the same manner, with non-clay minerals embedded in a clay matrix, showing similar mineral phase internal porosities (Table 2) and pore morphologies (Fig. 11). Zooming into the clay matrix (Fig. 10), shows the same characteristic microstructure inside the clay matrix for all samples investigated. Characteristic mineral phase internal pore morphologies coincide with already described pore-types in clay (Desbois et al., 2009 and Houben et al., 2013 for type I, II and III pores), as well as in non-clay mineral phases (such as pyrite, mica, quartz, feldspar and titanium oxide; Loucks et al., 2009 and 2012; Desbois et al., 2011b; Heath et al., 2011; Klaver et al., 2012 and Houben et al., 2013). Intra-granular pores in quartz and feldspar were interpreted as fluid inclusions. These observations suggest that at

the scale of the BIB-SEM investigations, Boom Clay shows homogeneous mineral phase internal microstructures, including porosity, and moreover, that the different mineral phases can be considered as 'elementary building blocks', which contribute to the overall Boom Clay microstructure, if combined. This concept has already been proposed by Desbois et al. (2011a, b) and Houben et al. (2013); however, inter-aggregate pores, as well as the very large pores found in sample EZE64 (Fig. 9), are additional elements of a microstructural model of the Boom Clay. One way to integrate larger inter-aggregate pores into the model, would be to link them to the proportion of clay to non-clay mineral phases, as well as the grain size of the sample.

We have shown that the contribution of inter-aggregate pores to the total observed porosity is clearly linked to and increasing with the grain size of a sample, as well as the non-clay mineral content (Tables 1 and 2). Moreover, the location of inter-aggregate pores within a sample seems to be controlled by clay – non clay interfaces (Figs 6-12). For the very large pores found in sample EZE64, which are internally coated with a material of kaolinitic composition and oriented sub-perpendicular to the sample bedding (Figs 9, 11e, 12a, b and 14e), we so far have not found any explanation or evidence in the literature, other than secondary porosity, related to the burial of material and the onset of diagenetic processes (Schmidt & McDonald, 1979; Johnston & Johnson, 1987 and Wilson & McBride, 1988). However, this explanation is unlikely in the case of the Boom Clay Formation, since the material has never been buried much deeper than its present depth (~200-300 m).

The preferred orientation of pores within the clay matrix along the bedding in the two fine-grained samples (EZE54 and EZE55; Fig. 14a, b), was interpreted to be a result of depositional, burial and compaction processes in the Boom Clay Formation. In the two coarse-grained samples (EZE52 and EZE64; Fig. 14c-e), pores in the clay matrix are not oriented preferentially along the bedding, suggesting that the framework of rigid clasts prevents the bedding-parallel alignment of clay minerals during deposition, burial and compaction. Due to the much smaller grain size and higher clay content (~50-60 wt.-%) in samples EZE54 and EZE55, the local changes in the strain field around rigid clasts do not have a major impact on the overall alignment of the clay minerals and the bedding parallel preferred orientation of pores in the clay matrix, although some deviation of the orientation of pores in the clay matrix, around rigid clasts, could also be observed in the two fine-grained samples (Fig. 12c).

Are pore sizes in the clay matrix power-law distributed?

Pore-size distributions in argillaceous materials have been previously fitted using power-laws (Desbois et al., 2009; Klaver et al., 2012; Houben et al., 2013). Using a non-linear binning, pore sizes (areas) of type I, II and III pores, measured in the

present study within the clay matrix show power-law distributions over several orders of magnitude, with comparable exponents (between 1.56-1.66) for all samples investigated (Fig. 13, left side). The complementary cumulative probability distributions of these pore-areas give slightly higher power-law exponents between 1.66-1.74, but still similar for all samples investigated. The difference between the results obtained from least square linear regression analysis and complementary cumulative probability distribution (CCD) calculation, was interpreted to be due to errors occurring as a result of the non-linear binning, used during linear regression analysis, especially towards larger pore sizes (Newman, 2006; Clauset et al., 2009). Thus, the power-law exponents obtained from the calculation of CCDs can be assumed to be more accurate. The power-law behaviour of pore sizes over several orders of magnitude implies a self-similar geometry of the pore space in Boom Clay, within the clay matrix, as well as a similar origin of porosity in all samples investigated, independent of sample origin, grain-size distribution and mineralogy. Moreover, the results allow extrapolating the measured pore-size distributions, below the limit of pore detection resolution and the resolution limit of MIP, to estimate total porosities in clay. However, above certain pore sizes, the complementary cumulative probability distributions of pore-areas show a deviation from the fitted power-law distributions (Fig. 13, right side). We interpret this to be due to the non representative detection and segmentation of larger pores during BIB-SEM investigations, as a result of the limited size of cross-section areas, which could be investigated at a sufficiently high magnification, within a practical time-frame. Here, additional studies at lower magnifications on larger BIB-polished areas, or micro-CT studies, are recommended.

Comparison of BIB-SEM and MIP porosities to literature data

Total visible porosities from BIB-SEM investigations (~10-20% of the analysed areas) are considerably lower than bulk sample porosities measured in the present study by MIP (~27-35 Vol.-%), or calculated water content porosities (~36-39 Vol.-%). Literature data on bulk porosities in Boom Clay are compatible with these results: e.g. Merceron (1994) or Boisson (2005) calculated water content porosities between 36-39 Vol.-%; Al-Mukhtar et al. (1996), Boisson (2005) and Dehandschutter et al. (2005) measured porosities between 27-35 Vol.-% from MIP; Bruggeman et al. (2009) and Aertsens et al. (2005a, b) found porosities between 34-40 Vol.-% using HTO-diffusion experiments, and porosities ~38 Vol.-% are reported in FUNMIG (2008) based on density difference calculations. Higher porosities from water content measurements, HTO-diffusion experiments and density difference calculations, compared to MIP data, indicate that a significant part of the porosity in Boom Clay (~10-30 Vol.-%) is borne by pores with throats smaller than

3.6 nm in diameter, the smallest pore-throat size accessible by MIP. The difference in total porosities measured by BIB-SEM and MIP (~40 to 60 %) can be partly explained by the difference in pore detection limits of the two methods (BIB-SEM ~1,000 nm² pore area at a magnification of 30,000× and MIP ~10 nm² equivalent pore-throat-area); however, comparing total porosities measured by BIB-SEM to MIP values at the practical pore detection resolution of BIB-SEM, still shows a significant difference of ~30-40%, which can only be attributed to larger pores or cracks measured by MIP, which were not measured during BIB-SEM analysis in representative amounts. Much larger areas would have to be investigated to cover for these pores and even then, part of the porosity measured by MIP may be exceeding the range of pore sizes detectable using BIB-SEM. Moreover, it has been suggested by various authors (e.g. Horseman et al., 1996; Hildenbrand & Urai, 2003), that Mercury injection Porosimetry on clayey materials, besides filling the accessible pore space, might also result in a significant compression of the sample pore space and a compaction of the clay fabric, resulting in an erroneous measurement of porosity volumes. This may be the case in the low pressure regime, at an initial stage of the experiment (Penumadu & Dean, 2000), as well as at very high pressures (>400 MPa), towards the end of the injection procedure (Hildenbrand & Urai, 2003). Thus porosity volumes measured by MIP always have to be interpreted with caution. In a follow up study, we plan to inject several samples with a molten metal, similar to Mercury, and afterwards image the injected samples using the BIB-SEM method, to be able to directly observe, whether the pore space has really been filled by the metal or only been compressed.

Pore connectivity and conceptual model of the pores pace in fine- and coarse-grained Boom Clay

MIP results show that a significant part of the porosity in Boom Clay is connected over the full pore size range accessible by MIP (Fig. 15). But whereas in the most fine-grained sample (EZE54), pores <300 nm pore-throat diameter (equivalent pore-throat area ~7·10⁴ nm²) contribute to the major part of the interconnected pore space, in the most coarse-grained sample (EZE64), much larger pores (>9,000 nm pore-throat diameter; ~6·10⁷ nm² equivalent pore-throat area) mainly control the interconnected porosity volume. In the other fine-grained sample (EZE55), small pores (<300 nm pore-throat diameter; ~7·10⁴ nm² equivalent pore-throat area), as well as much larger pores (> 2,000 nm pore-throat diameter; ~3·10⁶ nm² equivalent pore-throat area) contribute to the interconnected porosity volume (Fig. 15b). This shows that a major part of the connected pore space measured by MIP, is below the PPR of the BIB-SEM method. However, for the most coarse-grained sample (EZE64), interconnections between larger single pores were observed from BIB-SEM investigations, in good agreement with the MIP results; suggesting that the connectivity of the pore

space in Boom Clay is mainly controlled by the grain size of the sample, as well as the clay vs. non-clay mineral content.

A more detailed inspection of the MIP data allows for a further interpretation of the pore space architecture in Boom Clay: the observed hysteresis in the intrusion vs extrusion curves from MIP (Fig. 15a) indicates high pore-body to pore-throat ratios (up to 50 in the two fine-grained samples and up to 100 in the coarse-grained sample) and an entrapment of Mercury inside the samples after drainage (Matthews et al., 1995; Abell et al., 1999; Moro & Böhni, 2002). This phenomenon is referred to as 'ink-bottle-effect', due to the ink-bottle-like shape of the pores (Diamond, 2000). As a result of this, the too slow or incomplete filling of larger pores at pressures corresponding to their actual pore-throat sizes, may lead to an erroneous attribution of larger pores to smaller pore sizes, filling at higher pressures, and a shift of the measured pore-throat size distributions towards smaller pores sizes (Romero & Simms, 2008). In the most coarse-grained sample (EZE64), the maximum pore-body to pore-throat ratio is twice the one measured for the two fine-grained samples, indicating that a part of the porosity in sample EZE64 is connected via pores with much smaller throats, relative to their pore-bodies. The entrapment of Mercury inside the samples is mirrored in the sample weight gains after drainage. Porosity volumes corresponding to sample weight gains are in good agreement with the residual porosities measured after pressure release.

Power-law analysis of the MIP data, using least square linear regression analysis, indicates a power-law distribution of pore-throat sizes in Boom Clay, with similar exponents ~2 for all samples investigated and over the entire pore-throat size range measured, without a distinction between pores in the clay matrix and other non-clay mineral phases (Fig. 15c). This substantiates the hypothesised power-law behaviour and self-similar characteristics of the pore space in Boom Clay.

Based on the 'Friesen-Mikula approach', several different porosity regimes could be identified in the Boom Clay samples investigated, due to significant variations of the intruded Mercury volumes per pressure change (Fig. 15d; Romero & Simms, 2008). Resulting changes in the surface fractal dimension D_s , indicate changes in the porosity regime, or intrinsic changes in the pore network architecture, which can either be a result of sample preparation techniques (e.g. sample drying), or due to mechanical alteration during the MIP experiment (i.e. sample compression). We interpret the variations of intruded Mercury volumes per pressure change as changes in the pore connectivity regime and to correspond to critical pore entry pressures (Urai et al., 2008).

All obtained surface fractal dimensions are between two and three, thus fulfilling the criteria of a surface fractal structure, as defined by Friesen & Mikula (1987) and Bartoli et al. (1999).

As a result of BIB-SEM microstructural observations and data, we propose the following: the connectivity of the pore space in fine-grained Boom Clay (cf. samples EZE54 and EZE55) is mainly

controlled by pores below the PPR of the BIB-SEM method, but most likely within the clay matrix, whereas an increasing grain size and non-clay mineral content promote the interconnectivity of larger, inter-aggregate pores (cf. sample EZE64). Moreover, an increasing grain size leads to larger pores of type III (within the clay matrix), in the strain-shadows of rigid clasts, as well as larger clay – non-clay mineral interfaces, possibly localising drying-induced damage of the microstructure (Klinkenberg et al., 2009; Heath et al., 2011).

To substantiate our model of the Boom Clay microstructure and to be able to confidently discriminate between pores of type III and drying artefacts, more detailed investigations are needed. Therefore, in the future, cryogenic BIB-SEM investigations on undried Boom Clay samples are anticipated, as well as Wood's metal injection experiments in combination with BIB-SEM studies, to be able to visualise the connectivity of the pore space in Boom Clay directly and to compare the results to MIP data. In a follow-up study, pores characterised in the present contribution in 2D, shall be investigated in 3D, using serial focussed ion beam (FIB) cross-sectioning in combination with SEM, as well as μ -CT. Inferred 3D pore space characteristics, total porosity volumes and volume porosity distributions should be compared to the present 2D observations, as well as MIP inferred, indirect bulk sample porosities. Moreover, since the comparison of MIP and water content porosities indicates that a significant part of the porosity in Boom Clay is below the resolution of MIP and thus as well BIB-SEM and FIB-SEM, additional studies, such as transmission electron microscopy (TEM), or small angle neutron scattering are needed to receive information on the small pore-size regime.

Conclusions

BIB-SEM nm-scale microstructural investigations in combination with Mercury injection Porosimetry, show that the pore space in fine- and coarse-grained, representative samples of the Boom Clay Formation (Mol-1 borehole, Belgium) can be modelled as a combination of characteristic microstructural features of different mineral phases (including porosity), together with larger inter-aggregate pores, occurring preferentially at the boundaries between clay matrix and non-clay mineral grains. The origin of these larger pores is still subject to discussion, but part of them might be induced by the drying of the samples. Different mineral phases show characteristic pore morphologies, mineral phase internal porosities and pore-size distributions in all different samples investigated. Total sample porosities, as well as the connectivity of the pore space seem to be controlled by and increase with the sample grain size and non-clay mineral content. Moreover, the location and distribution of larger non-clay mineral grains within a sample, appears to be linked to the location of the largest pores and thus as well control the spatial distribution of porosity within a sample. Size distributions of pores within the clay matrix,

accounting for the majority of pores measured by BIB-SEM, can be described using power-laws with constant exponents over several orders of magnitude and similar for all samples investigated, irrespective of the sample origin, grain-size distribution and mineralogical composition. This points towards self-similarity of the pore space in Boom Clay, the possibility of up-scaling of our observation made on a nm- to μ m-scale, and a similar origin of porosity in the different samples investigated. Furthermore, the results of the present study show that a major part of the total water content porosity in Boom Clay is below the practical pore resolution (PPR) of the BIB-SEM method ($<1,000 \text{ nm}^2$ pore area at 30,000 \times magnification) and even below the resolution of MIP ($<3.6 \text{ nm}$ pore throat diameter). BIB-SEM observations made within representative elementary areas of μm^2 size cannot be considered as representative of total bulk sample porosities, due to large pores and/or cracks probably existing on a larger scale. However, BIB-SEM results can be considered as representative at the scale of observation, and moreover may relate to structural features of the Boom Clay on a larger scale.

Acknowledgements

We would like to thank ONDRAF/NIRAS (Belgian agency for radioactive waste and fissile materials) for their close cooperation and providing funding of this study, as being part of the program on geological disposal of high-level and long-lived radioactive waste in Belgium, carried out by ONDRAF/NIRAS.

References

- Abell, A.B., Willis, K.L. & Lange, D.A., 1999. Mercury intrusion porosimetry and image analysis of cement-based materials. *Journal of Colloid and Interface Science* 211: 39-44. www.sciencedirect.com/science/article/pii/S002197998959860
- Adamic, L.A. & Huberman, B.A., 2002. Zipf's law and the internet. *Glottometrics* 3: 143-150. www.hpl.hp.com/research/idl/papers/ranking/adamicglottometrics.pdf
- Aertsens, M., Dierckx, A., Put, M., Moors, H., Janssen, K., Van Ravestyn, L., Van Gompel, M. & De Cannière, P., 2005a. Determination of the hydraulic conductivity, the product ηr of the porosity η and the retardation factor r , and the apparent diffusion coefficient D_p on Boom Clay cores from the Mol-1 drilling. Restricted Contract Report SCK-CEN-R-3503 (Mol, Belgium).
- Aertsens, M., Dierckx, A., Put, M., Moors, H., Janssen, K., Van Ravestyn, L., Van Gompel, M. & De Cannière, P., 2005b. Determination of the hydraulic conductivity, ηr and the apparent diffusion coefficient on Ieper Clay and Boom Clay cores from the Doel-1 and Doel-2b drillings. Restricted Contract Report R-3589, SCK-CEN (Mol, Belgium).

- Aertsens, M., Van Gompel, M., De Cannière, P., Maes, N. & Dierckx, A.**, 2008. Vertical distribution of H14C03 transport parameters in Boom Clay in the Mol-1 borehole (Mol, Belgium): Clays in natural and engineered barriers for radioactive waste confinement. *Physics and Chemistry of the Earth, Parts A/B/C*, 33, Supplement 1 33: 61-66. <http://publications.sckcen.be/dspace/handle/10038/1022>
- Al-Mukhtar, M., Belanteur, N., Tessier, D. & Vanapalli, S.K.**, 1996. The fabric of a clay soil under controlled mechanical and hydraulic stress states. *Applied Clay Science* 11: 99-115. www.sciencedirect.com/science/article/pii/S0169131796000233
- Baeyens, B., Maes, A. & Cremers, A.**, 1985. In-situ physico-chemical characterization of Boom Clay. *Radioactive Waste Management and the Nuclear Fuel Cycle* 6: 391-408.
- Bak, P.**, 1996. *How nature works: The science of self organized criticality*. Springer (New York), 212 pp.
- Bartoli, F., Bird, N.R.A., Gomendy, V., Vivier, H. & Niquet, S.**, 1999. The relation between silty soil structures and their Mercury Porosimetry curve counterparts: Fractals and percolation. *European Journal of Soil Science* 50: 9-22. <http://onlinelibrary.wiley.com/doi/10.1046/j.1365-2389.1999.00209.x/abstract;jsessionid=7121D5405928DFEC6B06624343B10CEE.d03t03>
- Bell, J., Boateng, A., Olawale, O. & Roberts, D.**, 2011. The influence of fabric arrangement on oil sand samples from the estuarine depositional environment of the upper McMurray Formation. *Search and Discovery Article 80197*. www.searchanddiscovery.com/abstracts/html/2011/ice/abstracts/abstracts057.html
- Bésuelle, P., Viggiani, G., Lenoir, N., Desrues, J. & Bornert, M.**, 2006. X-ray micro CT for studying strain localization in clay rocks under triaxial compression. In: Desrues, J., Viggiani, G. & Bésuelle, P. (eds): *Advances in X-Ray CT for Geomaterials*. 2nd International Workshop GeoX.ISTE Ltd. (London): 35-53; 453 pp. <http://onlinelibrary.wiley.com/doi/10.1002/9780470612187.ch2/summary>
- Boisson, J.Y.**, 2005. Clay club catalogue of characteristics of argillaceous rocks. Report NEA No. 4436. OECD/NEA (Paris), 72 pp. www.oecd-nea.org/rwm/reports/2005/nea4436-argillaceous-catalogue.pdf
- Bruggeman, C., Maes, N., Aertsens, M. & De Cannière, P.**, 2009. Titrated water retention and migration behaviour in Boom Clay. SFC1 level 5 report (NIROND-TR 2009-16E), ONDRAF/NIRAS (Brussels, Belgium).
- Bugani, S., Modugno, F., Łucejko, J.J., Giachi, G., Cagno, S., Cloetens, P., Janssens, K. & Morselli, L.**, 2009. Study on the impregnation of archaeological waterlogged wood with consolidation treatments using synchrotron radiation microtomography. *Analytical and Bioanalytical Chemistry* 395: 1977-1985. <http://link.springer.com/article/10.1007%2Fs00216-009-3101-5>
- Cerepi, A., Durand, C. & Brosse, E.**, 2002. Pore microgeometry analysis in low-resistivity sandstone reservoirs. *Journal of Petroleum Science and Engineering* 35: 205-232. www.sciencedirect.com/science/article/pii/S0920410502002449
- Clauset, A., Shalizi, C.R. & Newman, M.E.J.**, 2009. Power-law distributions in empirical data. *SIAM Review* 51: 661-703. <http://arxiv.org/abs/0706.1062>
- Cnudde, V., Dewanckele, J., Boone, M., De Kock, T., Boone, M., Brabant, L., Duser, M., De Ceukelaire, M., De Clerq, H., Hayen, R. & Jacobs, P.**, 2011. High-resolution X-ray CT for 3D petrography of ferruginous sandstone for an investigation of building stone decay. *Microscopy Research and Technique* 74: 1006-1017. www.ncbi.nlm.nih.gov/pubmed/21381150
- De Craen, M., Swennen, R., Keppens, E., Macaulay, C.I. & Kiriakoulakis, K.**, 1999. Bacterially mediated formation of carbonate concretions in the Oligocene Boom Clay of northern Belgium. *Journal of Sedimentary Research* 69: 1098-1106. <http://archives.datapages.com/data/sepm/journals/v66-67/data/069/069005/1098.HTM?doi=10.1306%2FD4268B17-2B26-11D7-8648000102C1865D>
- De Craen, M., Delleuze, D., Volckaert, G., Sneyers, A. & Put, M.**, 2000. The Boom Clay as natural analogue. SCK-CEN Final report to NIRAS/ONDRAF (1997-1999) R-3444. Waste & Disposal Department SCK-CEN (Mol, Belgium), 131 pp.
- De Craen, M., Wang, L., Van Geet, M. & Moors, H.**, 2004. Geochemistry of Boom Clay pore water at the Mol site. SCK-CEN scientific report BLG-990. Waste & Disposal Department SCK-CEN (Mol, Belgium), 181 pp.
- Decler, J., Viane, W. & Vandenberghe, N.**, 1983. Relationships between chemical, physical and mineralogical characteristics of the Rupelian Boom Clay, Belgium. *Clay Minerals* 18: 1-10. www.minersoc.org/pages/Archive-CM/Volume_18/18-1-1.htm
- Decler, J. & Viaene, W.**, 1993. Rupelian Boom Clay as raw material for expanded clay manufacturing. *Applied Clay Science* 8: 111-128. www.sciencedirect.com/science/article/pii/016913179390032V
- Dehandschutter, B., Gaviglio, P., Sizun, J.P., Sintubin, M., Vandycyke, S., Vandenberghe, N. & Wouters, L.**, 2005. Volumetric matrix strain related to intraformational faulting in argillaceous sediments. *Journal of the Geological Society (London)* 162: 801-813. <http://jgs.geoscienceworld.org/content/162/5/801.full>
- Desbois, G., Urai, J. & Kukla, P.A.**, 2009. Morphology of the pore space in claystones – evidence from BIB/FIB ion beam sectioning and cryo-SEM observations. *eEarth* 4: 15-22. www.electronic-earth-discuss.net/4/1/2009/eed-4-1-2009.html
- Desbois, G., Urai, J.L., Houben, M.E. & Sholokhova, Y.**, 2010a. Typology, morphology and connectivity of pore space in claystones from reference site for research using BIB, FIB and cryo-SEM methods. *EPJ Web of Conferences (European Physical Journal)* 6: 22005. www.epj-conferences.org/index.php?option=com_article&access=standard&Itemid=129&url=/articles/epjconf/abs/2010/05/epjconf_ICEM14_22005/epjconf_ICEM14_22005.html
- Desbois, G., Enzmann, F., Urai, J.L., Baerle, C., Kukla, P.A. & Konstanty, J.**, 2010b. Imaging pore space in tight gas sandstone reservoir: Insights from broad ion beam cross-sectioning. *EPJ Web of Conferences (European Physical Journal)* 6: 22022. www.epj-conferences.org/index.php?option=com_article&access=standard&Itemid=129&url=/articles/epjconf/abs/2010/05/epjconf_ICEM14_22022/epjconf_ICEM14_22022.html
- Desbois, G., Urai, J.L., Kukla, P.A., Konstanty, J. & Baerle, C.**, 2011a. High-resolution 3D fabric and porosity model in a tight gas sandstone reservoir: A new approach to investigate microstructures from mm- to nm-scale combining argon beam cross-sectioning and SEM imaging. *Journal of Petroleum Sciences and Engineering* 78: 243-257. www.sciencedirect.com/science/article/pii/S0920410511001306
- Desbois, G., Urai, J., Houben, M., Hemes, S. & Klaver, J.**, 2011b. BIB-SEM of representative area clay structures: Insights and challenges. *NEA Clay Club Workshop Proceedings – Clay Under Nano- to Microscopic resolution – NEA OECD*, Sept. 6-8, 2011 (Karlsruhe).

- Desbois, G., Urai, J., Kukla, P., Wollenberg, U., Pérez-Willard, F., Radi, Z. & Riholm, S.**, 2012. Distribution of brine in grain boundaries during static recrystallization in wet, synthetic halite: Insight from broad ion beam sectioning and SEM observation at cryogenic temperature. *Contributions to Mineralogy and Petrology* 163: 19-31. <http://link.springer.com/article/10.1007%2Fs00410-011-0656-x>
- Desbois, G., Urai, J.L., Pérez-Willard, F., Radi, Z., Offern, S., Burkart, I., Kukla, P.A. & Wollenberg, U.**, 2013. Argon broad ion beam tomography in a cryogenic scanning electron microscope: A novel tool for the investigation of representative microstructures in sedimentary rocks containing pore fluid. *Journal of Microscopy* 249 (3): 215-235. <http://onlinelibrary.wiley.com/doi/10.1111/jmi.12011/abstract>
- Diamond, S.**, 1970. Pore size distributions in clays. *Clays and Clay Minerals* 18: 7-23. <http://clays.org/journal/archive/volume%2018/18-1-7.pdf>
- Diamond, S.**, 2000. Mercury porosimetry an inappropriate method for the measurement of pore size distributions in cement-based materials. *Cement and Concrete Composites* 30: 1517-1525. www.sciencedirect.com/science/article/pii/S0008884600003707
- ESRI**, 2011. ArcGIS Desktop: Release 10. Environmental Systems Research Institute (Redlands, CA).
- Fadeev, A.Y., Borisova, O.R. & Lisichkin, G.V.**, 1996. Fractality of porous silicas: A comparison of adsorption and porosimetry data. *Journal of Colloid and Interface Science* 183: 1-5. www.sciencedirect.com/science/article/pii/S0021979796905111
- Friesen, W.I. & Mikula, R.J.**, 1987. Fractal dimensions of coal particles. *Journal of Colloid and Interface Science* 120: 263-271. www.sciencedirect.com/science/article/pii/0021979787903481
- FUNMIG – Fundamental processes of radionuclide migration**, 2008. PID 3.2.1 Physical, mineralogical and geochemical characterization of the Boom Clay, Callovo-Oxfordian and Opalinus Clay rock samples, Contract No. FP6-516-514, 138 pp.
- Gens, R., Lalieux, P., De Preter, P., Dierckx, A., Bel, J., Boyazis, J.P. & Cool, W.**, 2003. The Second Safety Assessment and Feasibility Interim Report (SAFIR 2) on HLW Disposal in Boom Clay: Overview of the Belgian Programme. MRS Proceedings, 807, 917 (Belgium). <http://journals.cambridge.org/action/displayAbstract?fromPage=online&aid=8008166>
- Goldstein, M.L., Morris, S.A. & Yenj, G.G.**, 2004. Problems with fitting to the power-law distribution. *European Physical Journal B* 41: 255-258. <http://link.springer.com/article/10.1140%2Fepjpb%2Fe2004-00316-5>
- Griffault, L., Merceron, T., Mossmann, J.R., Neerdael, B., De Cannière, P., Beaucaire, C., Dumas, S., Bianchi, A. & Christen, R.**, 1996. Participation to the project archimede-argile. EEC Contract No. FI2W-CT90-0117, final report EUR 17454, ANDRA (France).
- Heath, J.E., Dewers, T.A., McPherson, B.J.O.L., Petrusak, R., Chidsey, T.C., Rinehart, A.J. & Mozley, P.S.**, 2011. Pore networks in continental and marine mudstones: Characteristics and controls on sealing behavior. *Geosphere* 7: 429-454. <http://geosphere.gsapubs.org/content/7/2/429.abstract>
- Hildenbrand, A. & Urai, J.L.**, 2003. Investigation of the morphology of pore space in mudstones – first results. *Marine and Petroleum Geology* 20: 1185-1200. www.sciencedirect.com/science/article/pii/S0264817203000904
- Holzer, L., Münch, B., Wegmann, M. & Gasser, P.**, 2006. FIB-nanotomography of particulate systems – part I: Particle shape and topology of interfaces. *Journal of the American ceramic society* 89: 2577-2585. <http://onlinelibrary.wiley.com/doi/10.1111/j.1551-2916.2006.00974.x/abstract>
- Holzer, L., Gasser, P., Kaech, A., Wegmann, M., Zingg, A., Wepf, R. & Münch, B.**, 2007. Cryo-FIB-nanotomography for quantitative analysis of particle structures in cement suspension. *Journal of Microscopy* 227: 216-228. <http://onlinelibrary.wiley.com/doi/10.1111/j.1365-2818.2007.01804.x/abstract?deniedAccessCustomisedMessage=&userIsAuthenticated=false>
- Holzer, L., Münch, B., Rizzi, M., Wepf, R., Marshall, P. & Graule, T.**, 2010. 3D-microstructure analysis of hydrated bentonite with cryo-stabilized pore water. *Applied Clay Science* 47: 330-342. www.sciencedirect.com/science/article/pii/S016913170900341X
- Holzer, L. & Cantoni, M.**, 2012. Review of FIB-tomography. In: Utke, I., Moshkalev, S. & Russell, P. (eds): *Nanofabrication using focused ion and electron beams: Principles and applications*. Oxford University Press (New York), 813 pp.
- Honty, M., De Craen, M., Wang, L., Madejová, J., Czimerová, A., Pentrák, M., Stríček, I. & Van Geet, M.**, 2010. The effect of high pH alkaline solutions on the mineral stability of the Boom Clay – batch experiments at 60° C. *Applied Geochemistry* 25: 825-840. www.sciencedirect.com/science/article/pii/S0883292710000739
- Horseman, S.T., Higgs, J.J.W., Alexander, J. & Harrington, J.F.**, 1996. Water, gas and solute movement through argillaceous media. The NEA (Nuclear Energy Agency) Working Group on Measurement and Physical Understanding of Groundwater Flow Through Argillaceous Media ('Clay Club'), a subgroup of the NEA Co-ordinating Group on Site Evaluation and Design of Experiments for Radioactive Waste Disposal (SEDE), Report 96/1 OECD, Paris, 290 pp.
- Houben, M.E., Desbois, G. & Urai, J.L.**, 2013. Pore morphology and distribution in the shaly facies of Opalinus Clay (Mont Terri, Switzerland): Insights from representative 2D BIB-SEM investigations on mm to nm scale. *Applied Clay Science* 71: 82-97. www.sciencedirect.com/science/article/pii/S0169131712002980
- Jackson, M.L.**, 1985. *Soil chemical analysis – advanced course*, revised 2nd edition, 11th printing. Parallel Press, University of Wisconsin – Madison Libraries (Madison, Wisconsin), 895 pp.
- Janssen, C., Wirth, R., Reinicke, A., Rybacki, E., Naumann, R., Wenk, H.R. & Dresen, G.**, 2011. Nanoscale porosity in SAFOD core samples (San Andreas Fault). *Earth and Planetary Science Letters* 301: 179-189. www.sciencedirect.com/science/article/pii/S0012821X1000693X
- Jin, G.**, 2007. Experimental validation of pore-level calculations of static and dynamic petrophysical properties of clastic rock. Society of Petroleum Engineers, 109547-MS. SPE International Annual Technical Conference and Exhibition, Nov. 11-14, 2007 (Anaheim, California, U.S.A.), 13 pp. www.onepetro.org/mslib/app/Preview.do?paperNumber=SPE-109547-MS&societyCode=SPE
- Johnston, D.D. & Johnson, R.J.**, 1987. Depositional and diagenetic controls on reservoir quality in first Wilcox Sandstone, Livingston Field, Louisiana. *American Association of Petroleum Geologists* 71: 1152-1161. <http://archives.datapages.com/data/bulletns/1986-87/data/pg/0071/0010/1150/1152.htm>

- Kameda, A., Dvorkin, J., Keehm, Y., Nur, A. & Bosl, W.**, 2006. Permeability-porosity transforms from small sandstone fragments. *Geophysics* 71: N11-N19. www.intl-geophysics.geoscienceworld.org/content/71/1/N11.full
- Keller, L.M., Holzer, L., Wepf, R. & Gasser, P.**, 2011. 3D geometry and topology of pore pathways in Opalinus Clay: Implications for mass transport. *Applied Clay Science* 52: 85-95. www.sciencedirect.com/science/article/pii/S0169131711000573
- Kemball, C.**, 1946. On the surface tension of Mercury. *Transactions of the Faraday Society* 42: 526-537. <http://pubs.rsc.org/en/content/articlepdf/1946/ft/ft9464200526>
- Klaver, J., Desbois, G., Urai, J.L. & Littke, R.**, 2012. BIB-SEM study of the pore space morphology in early mature Posidonia Shale from the Hils Area, Germany. *International Journal of Coal Geology* 103: 12-25. www.sciencedirect.com/science/article/pii/S0166516212001747
- Klinkenberg, M., Kaufhold, S., Dohrmann, R. & Siegesmund, S.**, 2009. Influence of carbonate microfabrics on the failure strength of claystones. *Engineering Geology* 107: 42-54. www.sciencedirect.com/science/article/pii/S001379520900101X
- Kolor**, 2012. Autopano Giga 2.6.1 (Challes-les Eaux, France).
- Korvin, G.**, 1992. *Fractal models in the earth sciences*. Elsevier (Amsterdam), 396 pp.
- Laenen, B.**, 1997. The geochemical signature of relative sea-level cycles recognized in the Boom Clay (PhD-thesis). Katholieke Universiteit Leuven, Faculteit Wetenschappen, Departement Geografie – Geologie (Leuven, Belgium), 396pp.
- Lexa, O., Štípská, P., Schulmann, K., Baratoux, L. & Kröner, A.**, 2005. Contrasting textural record of two distinct metamorphic events of similar p-T conditions and different durations. *Journal of Metamorphic Geology* 23: 649-666. <http://onlinelibrary.wiley.com/doi/10.1111/j.1525-1314.2005.00601.x/abstract>
- Locks, R.G., Reed, R.M., Ruppel, S.C. & Jarvie, D.M.**, 2009. Morphology, genesis, and distribution of nanometer-scale pores in siliceous mudstones of the Mississippian Barnett Shale. *Journal of Sedimentary Research* 79: 848-861. <http://josedres.sepmonline.org/content/79/12/848.abstract>
- Locks, R.G., Reed, R.M., Ruppel, S.C. & Hammes, U.**, 2012. Spectrum of pore types and networks in mudrocks and a descriptive classification for matrix-related mudrock pores. *AAPG Bulletin* 96: 1071-1098. <http://aapgbull.geoscienceworld.org/content/96/6/1071.abstract>
- MATLAB**, 2011. Version 7.12.0.635 (R2011a). The MathWorks Inc. (Natick, Massachusetts, U.S.A).
- Mandelbrot, B.**, 1982. *The fractal geometry of nature*. W.H. Freeman (New York), 468 pp.
- Matthews, G.P., Ridgway, C.J. & Spearing, M.C.**, 1995. Void space modeling of Mercury intrusion hysteresis in sandstone, paper coating, and other porous media. *Journal of Colloid and Interface Science* 171: 8-27. www.sciencedirect.com/science/article/pii/S0021979785711460
- Merceron, T.**, 1994. Characterisation of the geochemical environment of the Boom Clay at Mol. Archimedes – clay project, Proceedings MIRAGE meeting on the Migration of Radionuclides in the Geosphere, 3rd Phase, Nov. 15-17, 1994 (Brussels, Belgium).
- Meyer, K., Lorenz, P., Böhl-Kuhn, B. & Klobes, P.**, 1994. Porous solids and their characterization methods of investigation and application. *Crystal Research and Technology* 29: 903-930. <http://onlinelibrary.wiley.com/doi/10.1002/crat.2170290702/abstract>
- Moro, F. & Böhni, H.**, 2002. Ink-bottle effect in Mercury intrusion Porosimetry of cement-based materials. *Journal of Colloid and Interface Science* 246: 135-149. www.sciencedirect.com/science/article/pii/S0021979701979627
- Neuzil, C.E.**, 1994. How permeable are clays and shales? *Water Resource Research* 30: 145-150. <http://onlinelibrary.wiley.com/doi/10.1029/93WR02930/abstract>
- Newman, M.E.J.**, 2006. Power laws, pareto distributions and zipf's law. *Contemporary Physics* 46: 323-351. <http://arxiv.org/abs/cond-mat/0412004>
- Nicholas, M.E., Joyner, P.A., Tessem, B.M. & Olson, M.D.**, 1961. The effect of various gases and vapors on the surface tension of Mercury. *The Journal of Physical Chemistry* 65: 1373-1375. <http://pubs.acs.org/doi/abs/10.1021/j100826a023>
- ONDRAF/NIRAS**, 2011. Waste plan for the long-term management of conditioned high-level and/or long-lived radioactive waste and overview of related issues. Report NIROND 2011-02 E; Belgium, 255 pp. www.ondraf-plandecheets.be/nieuw/downloads/Waste%20plan%20-%20English.pdf
- Ortiz, L., Volckaert, G. & Mallants, D.**, 2002. Gas generation and migration in Boom Clay, a potential host rock formation for nuclear waste storage. *Engineering Geology* 64: 287-296. www.sciencedirect.com/science/article/pii/S0013795201001077
- Pareto, V.**, 1896-1897. *Cours d'économie politique*. Rouge, F. (Lausanne) & Pichon, F. (Paris), Vol. I-II: 430; 426 pp.
- Penumadu, D. & Dean, J.**, 2000. Compressibility effect in evaluating the pore-size distribution of kaolin clay using mercury intrusion porosimetry. *Canadian Geotechnical Journal* 37 (2): 393-405. www.nrcresearchpress.com/doi/abs/10.1139/t99-121#Uih73jj_kwxw
- Romero, E., Gens, A. & Lloret, A.**, 1999. Water permeability, water retention and microstructure of unsaturated compacted Boom Clay. *Engineering Geology* 54: 117-127. www.sciencedirect.com/science/article/pii/S0013795299000678
- Romero, E. & Simms, P.**, 2008. Microstructure investigation in unsaturated soils: A review with special attention to contribution of Mercury intrusion Porosimetry and environmental scanning electron microscopy. *Geotechnical and Geological Engineering* 26: 705-727. <http://link.springer.com/article/10.1007%2Fs10706-008-9204-5?LI=true>
- Ruffett, C., Gueguen, Y. & Darot, M.**, 1991. Complex conductivity measurements and fractal nature of porosity. *Geophysics* 56: 758-768. <http://geophysics.geoscienceworld.org/content/56/6/758.abstract>
- Schmidt, V. & McDonald, D.A.**, 1979. The role of secondary porosity in the course of sandstone diagenesis. *SEPM Special Publications (Aspects of diagenesis)* 26: 175-207. http://archives.datapages.com/data/sepmsp/SP26/The_Role_of_Secondary_Porosity.html
- Sigal, R.F.**, 2009. A methodology for blank and conformance corrections for high pressure Mercury Porosimetry. *Measurement Science and Technology* 20, 11 pp. <http://iopscience.iop.org/0957-0233/20/4/045108>
- Sok, R.M., Varslot, T., Ghous, A., Latham, S., Sheppard, A.P. & Knackstedt, M.A.**, 2009. Pore scale characterization of carbonates at multiple scales: Integration of micro-CT and FIB-SEM. *International Symposium of the Society of Core Analysts*, Sept., 27-30, 2009 (Noordwijk, the Netherlands), 12 pp. www.scaweb.org/assets/papers/2009_papers/SCA2009-18.pdf

- Turcotte, D.L.**, 1997. Fractals and chaos in geology and geophysics, 2nd edition. Cambridge University Press (Cambridge, UK): 398 pp.
- Urai, J.L., Nover, G., Zwach, C., Ondrak, R., Schöner, R. & Kroos, B.M.**, 2008. Transport processes. Dynamics of complex intracontinental basins: The central european basin system. Springer, Berlin-Heidelberg: 367-388.
- Van Geet, M., Bastiaens, W. & Ortiz, L.**, 2008. Self-sealing capacity of argillaceous rocks: Review of laboratory results obtained from the SELFRAC project. Physics and Chemistry of the Earth 33: S396-S406. www.sciencedirect.com/science/article/pii/S1474706508002891
- Vandenbergh, N.**, 1974. Een sedimentologische studie van de Boomse klei, doctorale verhandeling/Unpublished PhD thesis, Catholic University (K.U.) Leuven, 187 pp.
- Vandenbergh, N.**, 1978. Sedimentology of the Boom Clay (Rupelian) in Belgium. Verhandeling Koninklijke Academie voor Wetenschappen, Letteren en Schone Kunsten van België, Klasse Wetenschappen XL/147. Paleis der Academies (Brussels, Belgium), 137 pp.
- Verhoef, E. & Schröder, T.**, 2011. Research Plan. OPERA-PG-COV004. COVRA N.V. (the Netherlands), 52 pp.
- Verhoef, E., Neeft, E., Grupa, J. & Poley, A.**, 2011. Outline of a disposal in clay. OPERA-PG-COV008. COVRA N.V. (the Netherlands), 23 pp.
- Washburn, E.W.**, 1921. The dynamics of capillary flow. Physical Review 17: 273. http://prola.aps.org/abstract/PR/v17/i3/p273_1
- Webb, P.A.**, 2001. An introduction to the physical characterization of materials by Mercury intrusion Porosimetry with emphasis on reduction and presentation of experimental data. Micromeritics Instrument Corporation (Norcross, Georgia, USA): 23 pp. www.micromeritics.com/Repository/Files/mercury_paper.pdf
- Wentworth, C.K.**, 1922. A scale of grade and class terms for clastic sediments. The Journal of Geology 30: 377-392. www.jstor.org/stable/30063207
- Wilson, J.C. & McBride, E.F.**, 1988. Compaction and porosity evolution of Pliocene sandstones, Ventura Basin, California. American Association of Petroleum Geologists 72: 664-681. <http://archives.datapages.com/data/bulletns/1988-89/data/pg/0072/0006/0650/0664.htm?doi=10.1306%2F703C8EFC-1707-11D7-8645000102C1865D>
- Wouters, L., Herron, M., Abeels, V., Hagood, M. & Strobel, J.**, 1999. Innovative applications of dual range fourier transform infrared spectroscopy to analysis of Boom Clay mineralogy. Aardkundige Mededelingen 9: 159-168.
- Zeelmaekers, E.**, 2011. Computerized qualitative and quantitative clay mineralogy: Introduction and application to known geological cases. Unpublished PhD thesis, Katholieke Universiteit (K.U.) Leuven. Groep Wetenschap en Technologie (Heverlee, Leuven), 397 pp.
- Zipf, G.K.**, 1949. Human behaviour and the principle of least effort – an introduction to human ecology. Addison-Wesley Press (Oxford) England, 573 pp.